

## Article

# Surface Modification of Ti–30Ta Alloy by Deposition of P(VDF-TrFE)/BaTiO<sub>3</sub> Coating for Biomedical Applications

Larissa Mayra Silva Ribeiro <sup>1</sup>, Luziane Aparecida Costa da Rosa Simões <sup>1</sup>, Melina Espanhol-Soares <sup>1</sup>, Vinicius Carvalho Teles <sup>2</sup>, Tainara Aparecida Nunes Ribeiro <sup>1</sup>, Patrícia Capellato <sup>1,\*</sup>, Lucas Victor Benjamim Vasconcelos Fré <sup>1</sup>, Bruna Horta Bastos Kuffner <sup>1</sup>, Stephen Edward Sadow <sup>3</sup>, Daniela Sachs <sup>1</sup>, Ana Paula Rosifini Alves Claro <sup>4</sup> and Rossano Gimenes <sup>1</sup>

<sup>1</sup> Physics and Chemistry Department, Universidade Federal de Itajubá—UNIFEI, Itajubá 37500-903, Brazil

<sup>2</sup> Mechanical Engineering Department, Universidade Federal de Ouro Preto—UFOP, Ouro Preto 35400-000, Brazil

<sup>3</sup> Electrical Engineering Department, University of South Florida, Tampa, FL 33620, USA

<sup>4</sup> Materials and Technology Department, Universidade Estadual Paulista—UNESP, Guaratingueta 12516-410, Brazil

\* Correspondence: capellato@unifei.edu.br



**Citation:** Ribeiro, L.M.S.; Costa da Rosa Simões, L.A.; Espanhol-Soares, M.; Carvalho Teles, V.; Ribeiro, T.A.N.; Capellato, P.; Vasconcelos Fré, L.V.B.; Kuffner, B.H.B.; Sadow, S.E.; Sachs, D.; et al. Surface Modification of Ti–30Ta Alloy by Deposition of P(VDF-TrFE)/BaTiO<sub>3</sub> Coating for Biomedical Applications. *Metals* **2022**, *12*, 1409. <https://doi.org/10.3390/met12091409>

Academic Editor: Alexandre Emelyanenko

Received: 1 May 2022

Accepted: 12 July 2022

Published: 26 August 2022

**Publisher's Note:** MDPI stays neutral with regard to jurisdictional claims in published maps and institutional affiliations.



**Copyright:** © 2022 by the authors. Licensee MDPI, Basel, Switzerland. This article is an open access article distributed under the terms and conditions of the Creative Commons Attribution (CC BY) license (<https://creativecommons.org/licenses/by/4.0/>).

**Abstract:** This study aims to promote an adequate methodology for coating an experimental Ti-30Ta alloy with P(VDF-TrFE)/BaTiO<sub>3</sub>. The combination of a copolymer with a ceramic has not been used until now. Ti-30Ta is an excellent choice to replace current alloys in the global market. The composite deposition on the Ti-30Ta substrate was performed by a spray coating process and at low temperature using two different surface modifications: surface acidic etching and surface polishing. Characterization was divided into four areas: (I) the substrate surface treatments used and their influences on the adhesion process were evaluated using surface energy, wettability, and roughness analyses; (II) the properties of the composite film, which were carried out using X-ray diffractometry (XRD), Fourier transform infrared spectroscopy (FTIR), thermogravimetric analysis (TG), and differential scanning calorimetry (DSC); (III) the study of the adhesion of the film on the substrate, which was performed by a scratch test; (IV) the final product, which was evaluated to determine the surface properties after the coating process. Biofilm formation using *Staphylococcus aureus* and *Staphylococcus epidermidis* strains and a hemocompatibility test were performed as biological assays. The results indicated that the P(VDF-TrFE)/BaTiO<sub>3</sub> film showed high thermal stability (up to ≈450 °C); the FTIR and DSC tests indicated the presence of the β phase, which means that the material presents a piezoelectric nature; and the scratch test showed that the samples with the polish treatment provided a better adhesion of the film with an adhesion strength of ~10 MPa. From the SEM analysis, it was possible to determine that the spray deposition coating process resulted in a well-applied film as evidenced by its homogeneity. Microbiological tests showed that for *Staphylococcus aureus*, the bacterial growth in the coated Ti-30Ta presented no significant differences when compared to the alloy without coating. However, for *Staphylococcus epidermidis*, there was considerable growth on the coated Ti-30Ta, when compared to the non-coated alloy, indicating that the film surface may have favored bacterial growth. The hemolysis assay showed that the coated material presents hemocompatible characteristics when in contact with blood cells. The results obtained indicate that the Ti-30Ta alloy coated with P(VDF-TrFE)/BaTiO<sub>3</sub> is a promising alternative for implant applications, due to its biocompatible properties, simplicity, and low cost.

**Keywords:** Ti-30Ta alloy; P(VDF-TrFE)/BaTiO<sub>3</sub> composite; spray coating; surface characterization; biofilm adhesion

## 1. Introduction

Commercially-pure titanium (cp-Ti) and its alloys are widely used as implants and prostheses for substitution, fixation, or regeneration of bone tissue, due to their excellent

properties such as chemical stability, high mechanical strength, high biocompatibility, low Young's modulus, as well as good corrosion and fatigue resistance. These characteristics provide fast recovery and improve patient quality of life [1–3]. The biocompatibility of cp-Ti is a consequence of its low electrical conductivity, which influences the electrochemical oxidation of the surface itself, and promotes a passive layer of oxide that provides corrosion resistance [4].

Despite these aspects, cp-Ti has a bioinert nature, which means that the presence of this metal does not stimulate a tissue reaction, being indifferent to the biological environment [4]. It occurs because the non-treated surface of cp-Ti is not able to induce new bone formation during the initial healing process [5]. Furthermore, the elastic modulus of cp-Ti ( $\approx 110$  GPa) is higher than that of bone ( $\approx 10$ – $40$  GPa). This difference impairs the functionality of the implant and the tissue, leading to the possibility of fatigue and bone resorption [6,7].

To enhance the properties of metallic biomaterials, several titanium alloys have been studied over the years. Thus, the binary system Ti-Ta presents both combinations of titanium and tantalum (Ta), promoting a decrease in elastic modulus when compared to cp-Ti [8,9]. Tantalum is a refractory metal that does not present adverse effects on patient organisms. It has high applicability in the implant field and, once employed at 30% of its proportion, this metal presents high corrosion resistance, excellent biocompatibility, and low elastic modulus ( $\approx 69$  GPa), exhibiting better compatibility with the bone when compared to cp-Ti [10,11].

In addition to the characteristics mentioned above, tantalum also has a potential characteristic to protect tissue against infections, mainly bacterial. One of the reasons for the inhibition of biofilms is believed to be related to tantalum's ability to osseointegrate [12–14]. Osteoblasts integrate and proliferate on the surface of the material, thus preventing the access of bacteria and other microorganisms with the potential for infection. Another reason related to the inhibition of bacteria can be associated with the surface chemistry and surface energy of tantalum, which makes it impossible for pathogenic microorganisms to approach [14–18]. Still, some authors believe that the low microbial adhesion on the tantalum surface is a consequence of its high wettability and high surface energy [18,19].

Unfortunately, there are challenges related to the osseointegration process using metallic alloys. Therefore the surface characteristics of the metal must be modified. A commonly applied surface modification technique is surface coating using bioactive films, which promotes bone formation through cellular proliferation and integration with implanted material [20,21]. Moreover, the coating process optimizes the surface characteristics by increasing the contact area and mitigating biofilm formation, thus favoring the formation of tissue at the interface of the bone-implant and improving the implant's long-term stability [22,23].

The development of bioactive properties on the implant surface is associated with several materials. Recent applications include the use of piezoelectric ceramics as the  $(\text{Ba,Ca})(\text{Zr,Ti})\text{O}_3$  on Ti6Al4V alloys [24]. Polymers associated with hydroxyapatite such as PTFE were also used to coat MgMnCe alloys used for resorbable implants [25]. PLLA films also were used to coat 316 stainless steel substrates to stimulate the bioactivity of the host bone tissue [26]. Polymeric materials with piezoelectric properties, such as PVDF and its copolymer P(VDF-TrFE), were studied with the purpose of coating metallic surfaces because they can provide electrostimulation in the bone and favor osteogenesis [27,28]. These polymers are easy to manufacture, possess great flexibility, low weight, and are considered nontoxic [29]. However,  $\text{BaTiO}_3$  is applied on a large scale due to its biocompatibility and ability to adhere to bone tissue, maintain a charged surface, and provide bone cell adhesion and proliferation. In addition, this ceramic material presents higher piezoelectricity than PVDF [30,31]. In this context, the combination of  $\text{BaTiO}_3$  with a copolymer creates a composite P(VDF-TrFE)/ $\text{BaTiO}_3$ , which has electrical characteristics that promote bone regeneration [27,32–34]. Considering these benefits and possible solutions, the purpose of the present study was to develop a low-cost methodology to coat Ti-30Ta alloys using P(VDF-TrFE)/ $\text{BaTiO}_3$  films by employing a spray coating technique at room temperature.

The goal was to achieve a homogeneous deposition and good adhesion between the film and the substrate, in order to improve the biofunctionality of this alloy with the biological tissue. According to previous works related to the evaluation of biocompatibility of P(VDF-TrFE)BaTiO<sub>3</sub> membranes developed by the research group led by Professor Gimenes, the surface of P(VDF-TrFE)BaTiO<sub>3</sub> was shown to be osteogenic. Supported by published findings [28,34], we assume that Ti-30Ta coated with P(VDF-TrFE)/BaTiO<sub>3</sub> film can provide an osteogenic surface.

## 2. Experimental Procedure

This work was divided into four topics for better comprehension: (I) the surface modifications needed to coat the Ti-30Ta alloy with a suitable adhesion, (II) studies of the film's properties, (III) the surface properties of the final product, and (IV) biological assays to assess their tissue compatibility.

### 2.1. Sample Preparation

Ti-30Ta samples were obtained from a combination of Ti (99%) to Ta (99%) through the melting process in an argon atmosphere. The product was re-melted ten times and held in the molten state for 4 min, approximately. After this process, the ingots were subjected to vacuum at 1100 °C for 86.4 ks. The alloy was then cold-worked using a rotary swaging process at 100 rpm in a CNC lathe (Centur 30S, ROMY, Brazil), as reported by Capellato et al. [35]. The Ti-30Ta was then cut in discs of 2 mm thickness and 13 mm diameter; cp-Ti samples were supplied from the Mechanical Institute of the Federal University of Itajubá and were adopted as a control group. The cp-Ti and Ti-30Ta samples were divided into two distinct groups according to their surface treatment: (I) polish surface treatment—achieved using silicon carbide sandpaper (#1200) in a metallographic sample grinding and polishing machine for 30 s; and (II) acid etching surface treatment—achieved using Kroll reagent (5 mL of HNO<sub>3</sub> + 3 mL of HF + 100 mL of H<sub>2</sub>O). The samples were immersed in a reagent solution for 1 min and then washed using distilled water. All samples of both groups were cleaned in an ultrasonic bath with distilled water + acetone for 30 min. After these processes, the samples were dried in an oven at 37 °C.

### 2.2. Characterization of the Ti-30Ta and cp-Ti Substrates after the Surface Treatments

The wettability of the samples was evaluated by the contact angle method to estimate the surface hydrophilicity after the polish and acid etching treatments. The surface wettability was analyzed by a sessile Easy Drop Shape Analyzer (Krüss Scientific, Hamburg, Germany). The volume of the drop was 10 µL of deionized water, the contact angle was acquired at three different positions over the sample surface and the mean value was provided after five measurements at room temperature.

Surface energy was calculated using the Fowkes equation, as seen in Equation (1) [36,37]:

$$((1 + \cos \theta) / 2) = \sqrt{\gamma_s^d \times \gamma_l^d} + \sqrt{\gamma_s^p \times \gamma_l^p} \quad (1)$$

which  $\theta$  represents the contact angle between the liquid and the surface,  $\gamma_l$  is the surface tension of the liquid,  $\gamma_l^d$  is related to the dispersive components of the liquid and  $\gamma_l^p$  correspond to the polar component of the liquid. The component  $\gamma_s^d$  is associated with surface solid parameters,  $\gamma_s^p$  is the polar component of the solid and  $\gamma_s$  is the total energy surface of the solid.

The values of  $\gamma_l$ ,  $\gamma_l^d$  and  $\gamma_l^p$  are given by the literature. The values of  $\gamma_s^d$  and  $\gamma_s^p$  were determined using a system of linear equations (Equations (2) and (3)). For this analysis, it was necessary to use two different liquids to determine the total surface energy. For this reason, the contact angle was measured with deionized water and ethylene glycol, and

the system of linear equations was solved. The surface tension parameters of water and ethylene glycol are described in Table 1, according to Xu et al. [37].

$$\sqrt{\gamma_s^d} + a \sqrt{\gamma_s^p} = b(1 + \cos \theta_1), \quad (2)$$

$$\sqrt{\gamma_s^d} + c \sqrt{\gamma_s^p} = d(1 + \cos \theta_2), \quad (3)$$

where  $a$ ,  $b$ ,  $c$ , and  $d$  are the relative coefficients of the liquids and  $\theta_1$  represents the contact angle for the distilled water and  $\theta_2$  represents the contact angle for the ethylene glycol, shown in Table 2.

**Table 1.** Surface tension parameters of water and ethylene glycol.

Liquid	Surface Tension (mN/m)		
	$\gamma_l^d$	$\gamma_l^p$	$\gamma_l$
Water	21.8	51	72.8
Ethylene Glycol	29	19	47.7

**Table 2.** Contact angle measured for surface energy calculus.

Samples	Contact Angle ( $\theta$ ) [°]			
	Water		Ethylene Glycol	
	Polish	Acid Etching	Polish	Acid Etching
cp-Ti	66.1	60.1	73.8	69.3
Ti-30Ta	61.2	63.3	68.8	65.4

According to Żenkiewicz [38] the values for  $a$ ,  $b$ ,  $c$ , and  $d$  can be described by:

$$a = \sqrt{\frac{\gamma_{l1}^p}{\gamma_{l1}^d}} \quad b = \frac{\gamma_{l1}}{2\sqrt{\gamma_{l1}^d}} \quad c = \sqrt{\frac{\gamma_{l2}^p}{\gamma_{l2}^d}} \quad d = \frac{\gamma_{l2}}{2\sqrt{\gamma_{l2}^d}}$$

Finally, the polar and dispersive components of the liquid can be obtained, and the total surface energy can be calculated by Equation (4).

$$\gamma_s = \gamma_s^p + \gamma_s^d \quad (4)$$

The surface roughness ( $R_a$ ) of the samples was measured using a Surface Roughness Tester (Mitutoyo Corporation, Kawasaki, Japan). Five measurements of each surface treatment were carried out, and the mean value was obtained. To confirm the measurements, the roughness was also studied using the Phenom ProX SEM (Thermo Fisher Scientific, Waltham, MA, USA) with simulation in AFM and the image was treated using the Scanning Probe Image Processor (Mountains SPIP, Lyngby, Denmark) software.

### 2.3. P(VDF-TrFE)/BaTiO<sub>3</sub> Preparation

Commercial BaTiO<sub>3</sub> (Sigma Aldrich, St. Louis, MO, USA) powder was sintered in a MUFLA oven SSFM (7Lab, Rio de Janeiro, Brazil) for 4 h at 1380 °C, avoiding the contamination induced by BaCO<sub>3</sub> formation. The synthesis of the composite was realized using 1.5 g of P(VDF-TrFE) (Arkema Piezotech, Lyon, France) dispersed in 10 mL of dimethylformamide (DMF) (Sigma Aldrich, St. Louis, MO, USA) at room temperature (25 °C). The P(VDF-TrFE) + DMF solution was solubilized with a magnetic stirrer, and after copolymer dissolution, 0.5448 g of BaTiO<sub>3</sub> was added to the solution. P(VDF-TrFE) + BaTiO<sub>3</sub> + DMF was mixed for 6 min using a high-power ultrasound tool VCX 750 (Sonic and Materials,

Newtown, CT, USA) under refrigeration in ice/water. This procedure has been performed to ensure that powder agglomerates would be better homogenized.

#### 2.4. Characterization of the P(VDF-TrFE)/BaTiO<sub>3</sub> Film

##### Thermal and Structural Evaluation

The samples used for these analyses were obtained by spraying the P(VDF-TrFE)/BaTiO<sub>3</sub> solution on distilled water until a thin membrane was formed. Using this process, the DMF is forced to migrate to water and the precipitation of the solution occurs forming a solid film.

Thermogravimetric analysis (TGA) and differential scanning calorimetry (DSC) were employed in order to evaluate the mass variation of P(VDF-TrFE)/BaTiO<sub>3</sub> film and its thermal phase transitions, respectively. The TGA was performed by a Shimadzu TGA-50 (Shimadzu do Brasil Ltd., Barueri, Brazil) tool, in the temperature range of 25–1000 °C with a heating rate of 10 °C/min. The DSC technique was accomplished in a Shimadzu DSC 60 Plus (Shimadzu do Brasil Ltd., Barueri, Brazil) tool at 25–250 °C, a heating rate of 10 °C/min, and N<sub>2</sub> as a purge gas at 50 mL/min.

The degree of crystallinity of the copolymer depends on the heat treatments involved to process it. The analysis of the crystallinity of both the copolymer and the membrane is important to evaluate the β phase of the material and study its influence on film piezoelectric properties. The degree of crystallinity ( $\Delta X_c$ ) was calculated using Equation (5) [39]:

$$\Delta X_c = \left( \frac{\Delta H_m}{\Delta H_{100}} \right) \times 100\%, \quad (5)$$

where  $\Delta H_m$  is the melting enthalpy of the copolymer obtained in the DSC analysis, and  $\Delta H_{100}$  corresponds to the melting enthalpy of the copolymer which presents 100% crystallinity. The crystallinity for the composite can be calculated using Equation (6) [40]:

$$\Delta X_c = \left( \frac{\Delta H}{\Delta H_m \left( 1 - \frac{\varphi}{100} \right)} \right) \times 100\%, \quad (6)$$

where  $\Delta H$  is the P(VDF-TrFE) melting enthalpy obtained in the DSC analysis,  $\Delta H_m$  is the melting enthalpy of the composite and  $\varphi$  corresponds to the weight (% wt) of the ceramic material on the composite.

Fourier transform infrared spectroscopy (FTIR) was employed to identify the conformation and structural phases of P(VDF-TrFE) and the possible changes in the structural phases of the copolymer after BaTiO<sub>3</sub> incorporation. FTIR measurement was carried out in a Perkin Elmer Spectrum 100 FT-IR Spectrometer (Perkin Elmer do Brasil, São Paulo, Brazil), in the range of 1500–800 cm<sup>-1</sup>, resolution at 4 cm<sup>-1</sup>, and 32 scans.

To determine the crystalline phases of the P(VDF-TrFE)/BaTiO<sub>3</sub> film, the X-ray diffraction XRD technique was applied. In addition, the XRD analysis allowed evaluation of the possible microstructural changes coming from the combination of the ceramic and polymeric powder on P(VDF-TrFE)/BaTiO<sub>3</sub> synthesis. XRD also evaluated if there were new phase formations after the coating process as well. XRD data were acquired using an X'Pert Pro Scanning Diffractometer (Malvern Panalytical, São Paulo, Brazil), Cu X-ray tube, and  $k\alpha$  filter. Scans were made over 10°–90° in  $2\theta$  and steps of 0.01° over 0.5 s for P(VDF-TrFE)/BaTiO<sub>3</sub> film and for Ti-30Ta/P(VDF-TrFE)/BaTiO<sub>3</sub>.

#### 2.5. P(VDF-TrFE)/BaTiO<sub>3</sub> Deposition on Ti-30Ta and cp-Ti Substrates

The deposition of P(VDF-TrFE)/BaTiO<sub>3</sub>/DMF solution on the substrate surface was executed employing the spray coating method, using a commercial airbrush 5 mm gun connected to a compressed-gas supply pressure working at 20 kgf/cm<sup>2</sup>. P(VDF-TrFE)/BaTiO<sub>3</sub>/DMF deposition was performed at a pattern distance from 30 mm of the Ti-30Ta and cp-Ti substrates, which were heated to 150 °C and maintained at this temperature during the coating process. At the same time, distilled water was simultaneously sprayed via aerosol

dispersion and, consequently, a precipitation of the solution was formed on the substrate. After the coating process, the coated samples were dried in an oven at 100 °C for 12 h under vacuum (15 mmHg). The deposition process can be seen in Figure 1.

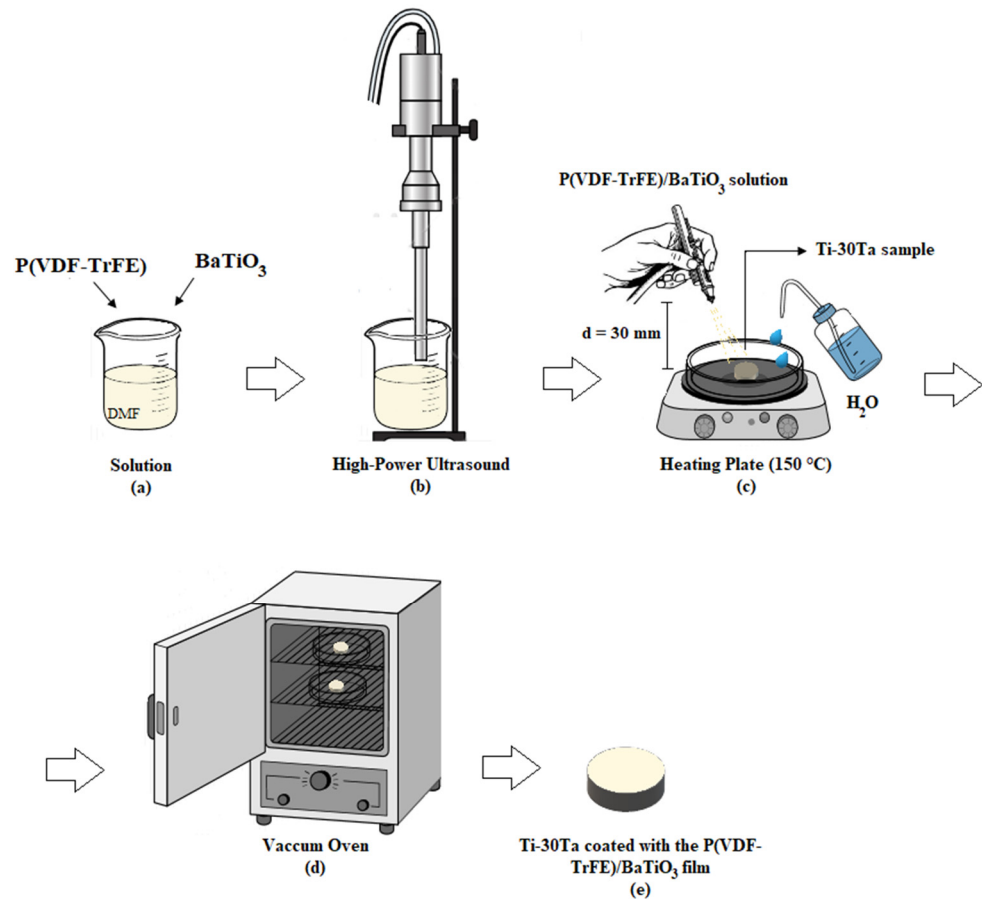


**Figure 1.** Illustrative coating process of cp-Ti and Ti-30Ta samples. (a) P(VDF-TrFE) and BaTiO<sub>3</sub> solubilization; (b) dispersion and disaggregation of BaTiO<sub>3</sub> particles in solution; (c) spray coating process; (d) samples dried in a vacuum oven; (e) final product obtained.

Film thickness was controlled by the deposition time associated with the homogeneity of the solution on the substrate. Several measurements of the thickness were performed using a digital micrometer to compare the thickness among the samples during the coating process and thus establish a standard coating time after the deposition of the film. The spraying time was adapted until a fluid layer of P(VDF-TrFE)/BaTiO<sub>3</sub> was obtained free from agglomerations; this was standardized to 60 s to achieve the thickness of a range of 10–20 µm. The dispersion flow rate was regulated according to the homogeneous distribution of the solution for the whole surface and the non-formation of crinkles onto the substrate.

## 2.6. Characterization of the Coated Ti-30Ta and cp-Ti Substrates

### 2.6.1. Adhesion Film on Substrate: Scratch Test

The adhesion between the coating and the substrate was evaluated by the scratch test, according to ASTM D7027-05E1 [41]. The device employed for this analysis was described in previous works [42,43]. For this test, a Rockwell C indenter was used and scratches of 3 mm in length were made. Normal load cell varied linearly from 0 N to 30 N. The scratch speed was 10 mm·min<sup>-1</sup>. Five measurements were taken, and an average value for the adhesion strength was calculated. The images of the scratches were obtained using an optical microscope BX51WI (Olympus Scientific Solutions, Tokyo, Japan).

## 2.6.2. Wettability, Surface Energy, and Roughness of the Coated Substrates

The surface wettability, surface energy, and roughness measurements were also obtained as previously described in Section 2.2 of this work. For the wettability assay, the absorption of the liquid on the surface of the coated substrate was analyzed by measuring the contact angle with a frequency of 20 min within a 60 min time window.

## 2.7. Biological Assays of the Coated Substrates

### 2.7.1. Biofilm Formation

Biofilm formation in coated and non-coated samples was realized using *Staphylococcus aureus* (ATCC 6538) and *Staphylococcus epidermidis* (ATCC 12228) strains, which are present in the bone mineralization stage for orthopedic and dental implants [44].

The strains were inoculated in Brain Heart Infusion Broth (BHI) for 24 h in an incubator at 37 °C. After the incubation period, the solution obtained was streaked in a Petri dish with agar and returned to the incubator for 24 h for biofilm formation. An aliquot of the bacterial colony was added in a 0.9% NaCl solution until the liquid medium concentration on the McFarland 0.5 scale ( $1.5 \times 10^8$  cells mL<sup>-1</sup>).

The samples were grouped into the control group, represented by the non-coated Ti-30Ta samples with polished surface treatment and the test group, represented by the Ti-30Ta coated samples. The test group was sterilized in UV for 30 min and the control group was polished with silicon carbide sandpaper (#1200), which provides a favorable environment for bacteria growth. After this process, the control samples were also sterilized in UV for 30 min. The samples were put in 12-well culture dishes with BHI and the McFarland suspension and placed in the incubator for 48 h at 37 °C. After this process, the samples were washed in phosphate-buffered saline (PBS) for 10 min and sonicated in a vortex for 3 min to remove any non-adherent biofilm on the sample surface. The resulting solution was diluted in 0.9% NaCl solution (pure, 10<sup>-2</sup>, 10<sup>-4</sup>, 10<sup>-6</sup>, and 10<sup>-8</sup>). Thus, a droplet of each dilution was inoculated in a Petri dish with agar and, finally, the plates were placed in the incubator for 24 h at 37 °C. From this process, the colonies grown on the surface samples were verified using Equation (7) and the colonies-forming unit (CFU) was calculated [45].

$$CFU \left( \text{mL}^{-1} \right) = \frac{n \text{ colonies}}{\text{sample dilution} \times \text{inoculated volume}} \quad (7)$$

### 2.7.2. Hemolysis Assay

According to ASTM F756-17, the hemolysis assay is considered a cytotoxicity test in vitro, which evaluates the biocompatibility of the material when in contact with blood cells. If the material presents non-hemocompatible properties, destructive changes occur in the cell through the disruption of the cell membrane, leading to the release of hemoglobin. A material can be classified as hemolytic or not using Table 3 [46].

**Table 3.** Defined rates for hemolysis occurrence.

Hemolytic Index *	Hemolytic Grade
0–2	Non-hemolytic
2–5	Slightly hemolytic
>5	Hemolytic

\* according to the negative control.

For this test, the samples were sterilized in UV for 30 min and then placed in Falcon tubes with 10 mL of 0.9% saline solution at 37 °C for 30 min to simulate a favorable environment for the red blood cells. The blood used for this procedure was collected from a healthy patient using a vacuum method.

The positive group (+), which represents 100% of hemolysis, was prepared by adding 0.2 mL of blood to 10 mL of distilled water. The control group (–), which represents 0% of hemolysis, was prepared by adding 0.2 mL of blood to 10 mL of 0.9% sodium chloride.

The collected blood was diluted in 5 mL of saline solution and an aliquot was incubated at 37 °C for 1 h. Posteriorly, the aliquot was centrifuged for 5 min at 2500× g in a centrifuge (Fisher Scientific, Pittsburgh, PA, USA). The absorbance of the supernatant was read in a spectrophotometer at a wavelength of 540 nm (Femto Industries, São Paulo, Brazil). After obtaining the absorbance of samples from both groups and the test samples, the hemolysis rate (%) could be calculated according to Equation (8) [47]:

$$R = \frac{(A - C_n)}{(C_p - C_n)} \times 100, \quad (8)$$

where  $A$  is the absorbance of the sample,  $C_n$  is the absorbance of the negative control and  $C_p$  is the absorbance of the positive control.

### 2.8. SEM Analysis

The surface treatments, such as the coating morphology and the biofilm growth, were performed using the Phenom ProX SEM (Thermo Fisher Scientific, Waltham, MA, USA). As there was a risk of the film rupturing during the segmentation of the sample, it was decided to analyze the cross-section of the coated sample through the interface between the coating and the substrate at the edge of the sample.

To analyze the biofilm distribution on the surface through SEM, the samples were immersed in a solution with glutaraldehyde 2% for fixation of the bacteria on the surface. After this process, the samples were rinsed with phosphate buffer saline. Then, the dehydration of the biofilm occurred in graded acetone with concentrations of 30%, 50%, 70%, 90%, and 100% for a 10-minute-bath per concentration. The samples were dried in an oven for 24 h and were finally coated with gold sputtering using a vacuum metallizer IC 60 (Shimadzu do Brasil Ltd., Barueri, Brazil) for 3 min with an electrical current of 6 mA.

### 2.9. Statistical Analysis

Statistical analysis was achieved using a two-way analysis of variance (ANOVA) and the T-Student test to evaluate the influence of the surface treatment on roughness, wettability, surface energy, adhesion strength, and the biological assays. The data were analyzed by GraphPad Prism 7, and all tests were conducted at a significance level of 0.05.

## 3. Results and Discussion

### 3.1. Characterization of the Ti-30Ta and cp-Ti Substrates after the Surface Treatments

The nature of the film and the substrate surface refers directly to the adhesive strength in the coating process, as well as how it was cured. From the moment that two different materials are arranged in intimate contact, a new interface is formed and the interaction between these materials will determine the bond strength between the surfaces [48]. The adhesion of thin films on metallic substrates occurs when the surface presents pores, scratches, voids, and cracks, which allows for film penetration and, consequently, a mechanical fixation at the interface of these materials [49].

A crucial parameter for coated surfaces is the bond strength of the film on the substrate. If an adhesive failure occurs, other film properties, such as biocompatibility and biofunctionality, will be lost due to particle release from the film in the biological environment [50]. For this reason, the coated surface must resist mechanical forces such as scratches, impacts, tensile/bending forces, and withstand the conditions imposed by the environment. Therefore, the surface characteristics before the coating process were assessed concerning the surface properties, such as topography, surface energy, roughness, and wettability in order to investigate their influence on the adhesion of the film to the substrate.

The topography of the treated samples before the coating process can be seen in Figure 2. In Figure 2a, the polished surface of the cp-Ti presents grooves throughout the surface. It is also possible to see the formation of valleys and peaks throughout the sample. The sample in Figure 2b represents the micrograph of the cp-Ti sample with acid etching

surface treatment, and grain boundaries can be seen (in light gray) separating regions with different crystallographic orientations ( $\alpha$  and  $\beta$  phases of titanium), revealed due to the effect of the Kroll's reagent. In addition, the presence of wrinkles was observed surrounding the whole surface. The arrangement of the elements that characterize a rough profile on the surface of the sample can be considered homogenous. However, there are some regions with a higher concentration of microcavities. This roughness pattern is responsible for characterizing the surface as isotropic, without preferential orientations of formed wrinkles. Figure 2c refers to the micrograph of Ti-30Ta alloy with inherent surface irregularities from the polishing process, with thin cracks aligned parallel in the transversal direction, characterizing a preferential orientation. Finally, the Ti-30Ta sample is present in Figure 2d, which represents the surface treated with acid etching. It is observed that there are grooves and micropores distributed throughout the sample. The difference in morphology of the cp-Ti and Ti-30Ta after the acid etching using Kroll's reagent can be explained by the dioxide layer on the cp-Ti surface, which is one of the most difficult materials to corrode. Kroll's reagent is the most efficient etchant employed on titanium alloys and can reveal the microstructure of these materials due to the presence of hydrofluoric acid and nitric acid, considered powerful oxidizing agents. Related to the Ti-30Ta surface, the reagent promoted a more eroded and corroded surface when compared to the cp-Ti due to the tantalum dissolving in hydrofluoric acid, where the passive layer of tantalum oxide is attacked strongly by this acid, leading to an increase in the surface oxidation.

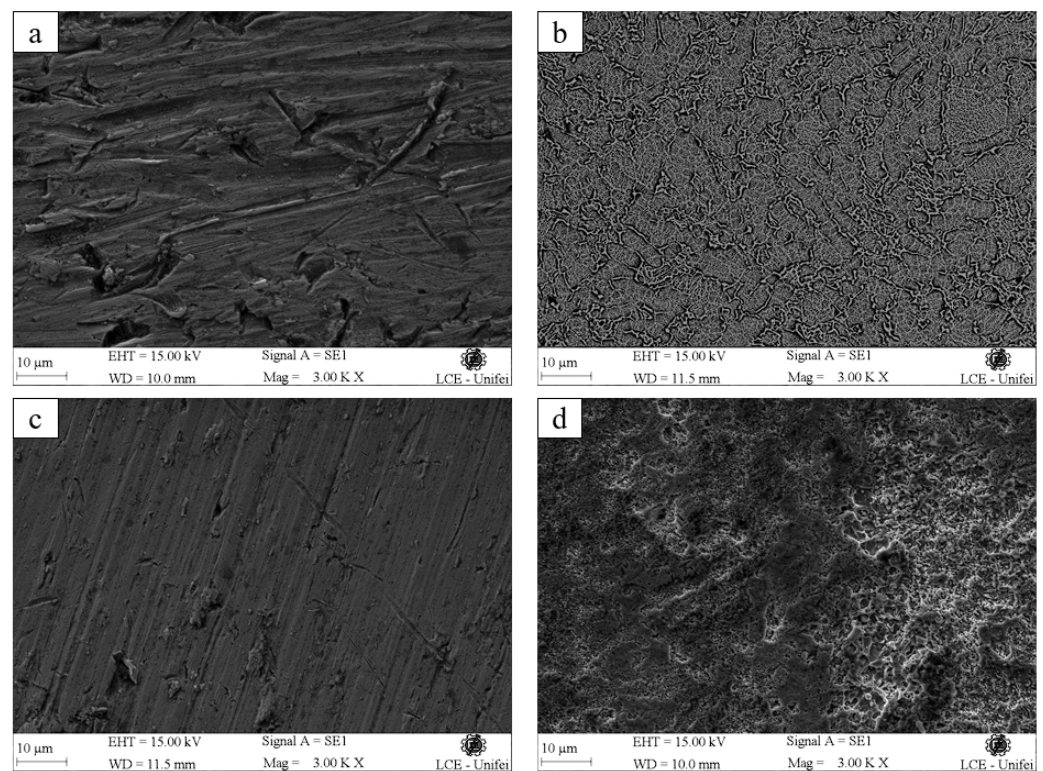


**Figure 2.** Topography of cp-Ti and Ti-30Ta samples: (a) cp-Ti sample after polish treatment; (b) cp-Ti after the acid etching process; (c) Ti-30Ta sample with polished surface treatment; (d) Ti-30Ta sample with acid etching treatment.

The advantage of abrasive surface treatments is related to the fact that the deposited film penetrates the irregularities formed, increasing the adhesion strength at the interface of the coating material and the substrate [48]. For this reason, surface treatments performed on the samples standardized the surface roughness to analyze the best surface treatment obtained in this work when associated with the adhesive strength of the P(VDF-TrFE)/BaTiO<sub>3</sub> coating film.

Obtained roughness data before the surface treatment are shown in Table 4. The study of the rough surface of metallic substrates before the coating process can be found in the works of Biasetto and Elsayed [51], Geng et al. [52], Zhou et al. [53], Guo et al. [54], and Cordeiro et al. [55], which possess  $R_a$  (arithmetical mean of surface roughness) values very similar to the values described for cp-Ti substrates presented in this work ( $R_a = 0.15 \mu\text{m}$ ). Analyzing the results, there was no significant difference between the roughness for polish or acid etching treatment.

**Table 4.** Non-coated cp-Ti and Ti-30Ta surface roughness.

Samples	Roughness $R_a$ ( $\mu\text{m}$ )	
	Polish	Acid Etching
cp-Ti	$0.150 \pm 0.05$	$0.260 \pm 0.08$
Ti-30Ta	$0.158 \pm 0.03$	$0.206 \pm 0.05$

According to ASTM C1624-05 [56], the roughness value for thin films formed by ceramic materials, with thickness  $\leq 30 \mu\text{m}$ , must present  $R_a < 0.5 \mu\text{m}$ . This range of values maintains the patterns defined by the ASTM standard, which guarantees the film adhesion on the substrate. As seen in Table 4, the values found for the surface roughness of all samples ( $0.1\text{--}0.25 \mu\text{m}$ ) are in accordance with the standard, since the value for the film thickness of this work was  $\approx 20 \mu\text{m}$  for all substrates. Choi et al. [48] have found in their studies that the relation between the surface roughness and the coating adhesion on a substrate refers to the increase in surface area. In other words, the surface roughness influences the interface between the substrate and the deposited film, improving the adhesion strength between both of them. Besides, the adhesion strength on rough surfaces may be adequate due to the high surface energy of atoms present on the scratched surface [57].

Figure 3 represents the contact angle measurements. According to the results, both substrates have absorptive characteristics, since the contact angle formed on the surface samples remains smaller than  $90^\circ$ , characterizing the surface of the samples as hydrophilic. The hydrophilicity or hydrophobicity is an intrinsic feature of wettability, which is a property associated with the surface energy of a material. Surfaces with high free energy are characterized by their hydrophilic nature, and the higher the surface energy of a material, the greater its ability to interact chemically with the liquid used [58]. The wettability of a surface can determine the success of the adhesion of the thin film to various substrates on account of the interface tension of the film in the liquid state and the surface energy of the substrate in a solid state. The adhesion strength between the two surfaces is determined by the interactive nature of both materials, which are dependent on wettability. The tension between the film and substrate interface determines the fixation of the coating on a solid surface, which means that hydrophilic surfaces provide better adhesion [19,48].

Table 5 shows the surface energy of cp-Ti and Ti-30Ta samples calculated before the coating process. Analyzing the data, there was a statistically significant difference in the surface energy for the polish treatment group when compared to the acid etching treatment group ( $p < 0.05$ ). These results indicated that the surface energy suffers changes related to the preparation of the substrate's surface. The surface energy of polished substrates presented values higher than substrates with acid etching treatment, suggesting that the polished surface is better than acid etching treatment.

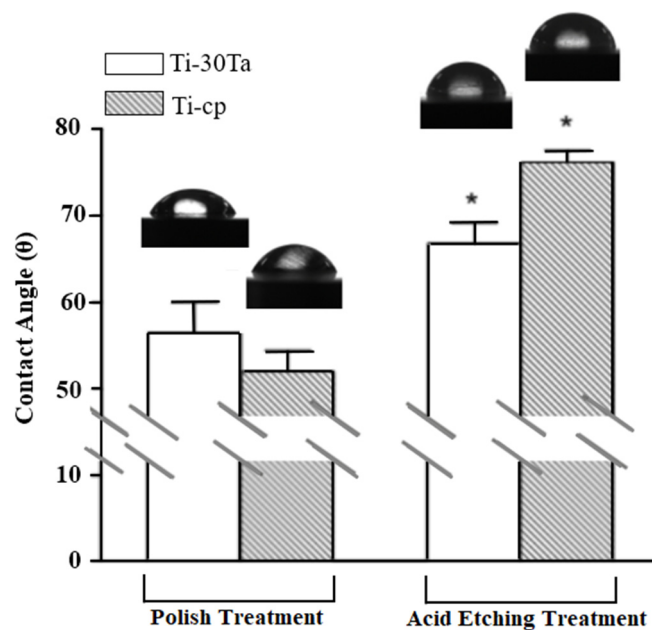


**Figure 3.** Water contact angle of cp-Ti and Ti-30Ta surface. \* indicates that the difference between the samples are statistically significant ( $p < 0.05$ ).

**Table 5.** Surface energy of the non-coated cp-Ti and Ti-30Ta samples.

Samples	Surface Energy $\gamma_s$ (mN/m)	
	Polish	Acid Etching
cp-Ti	$51.73 \pm 2.33$	$48.17 \pm 1.87$
Ti-30Ta	$57.33 \pm 1.35$	$48.49 \pm 4.71$

The relation between the surface energy and adhesion strength is given through the attraction and repulsion forces, which have polar and dispersive components. When the polar components are higher than the dispersive ones, a greater adhesion strength occurs between the film and substrate. This implies that the surface energy is directionally connected to surface adhesiveness and surfaces with high free energy promote a better interaction with the deposited film [18].

### 3.2. Evaluation of the P(VDF-TrFE)/BaTiO<sub>3</sub> Film

The thermal behavior of the P(VDF-TrFE)/BaTiO<sub>3</sub> films can be seen in Figure 4. The TGA profile curve obtained in this work is very similar to the P(VDF-TrFE) curve, as seen in previous works [59,60]. In the range from 25 °C to 160 °C, the TGA curve showed no significant mass losses. This event indicates that the solvent used in the composite synthesis was dried entirely since there are no peaks on the DTG curve between 140–160 °C, which refers to DMF evaporation. At 450–550 °C there was a weight loss of the composite, where around 67.5% of its mass was decomposed. The remaining weight of the compound is considered residual mass, which can be attributed to the addition of BaTiO<sub>3</sub> and residues from the copolymer process, as seen in Simões et al. (2010) [61]. Analyzing the derivative thermogravimetric curve (DTG) it is possible to identify events that are not seen by analyzing only the thermogram curve. The reaction reaches its maximum rate at 450 °C, and at 550 °C it is possible to observe a second lower intensity peak, indicating another weight loss process of the composite. The first DTG peak is assigned to the degradation of vinylidene fluoride, while the second peak is related to the degradation of trifluorethylene, since the mass loss (67.5%) at 450 °C is higher than the mass loss ( $\approx 33\%$ ) at 550 °C, reflecting the molar composition of the copolymer—VDF 80 mol% and TrFE 20% mol.

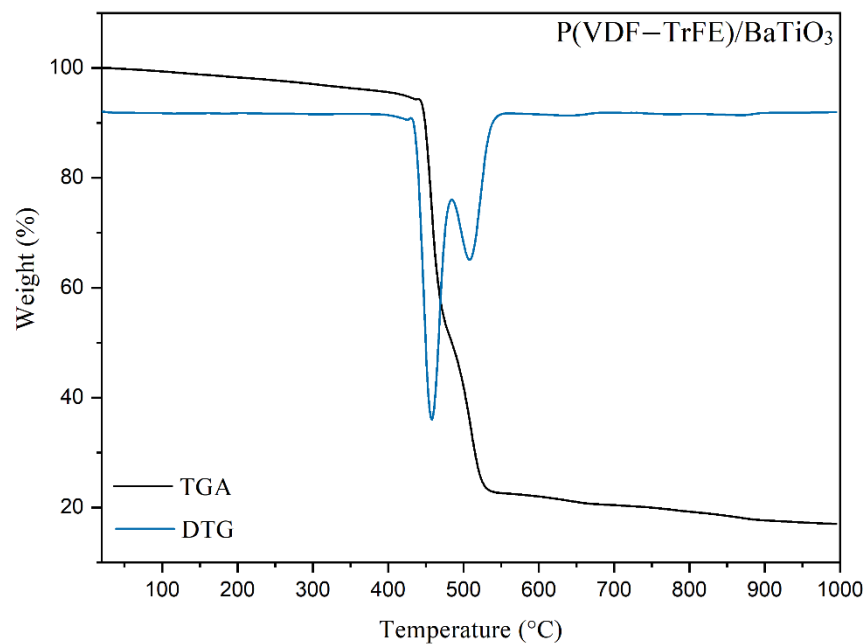


**Figure 4.** Thermal behavior of P(VDF-TrFE)/BaTiO<sub>3</sub> film and your derivative at 20 °C to 1000 °C.

By DSC analysis, the nature of the energy involved in endothermic and exothermic processes that occurred during the controlled temperature rise could be assessed. During the drying of the composite onto the metallic Ti-30Ta substrate the temperature employed will exert an influence on PVDF-TrFE chain orientation; further, the annealing at temperatures above the Curie temperature ( $T_c$ ) induces crystalline formation, and it will generate a higher piezoelectric effect on the film. The correct temperature for drying and annealing the film can be better determined after an investigation of the transition temperatures obtained by DSC. Figure 5 shows an endothermic peak at 88.46 °C, which corresponds to the Curie temperature ( $T_{c1}$ ) of the P(VDF-TrFE) copolymer. At 137.5 °C occurs a second phase transition ( $T_{c2}$ ), being similar to the copolymer catalog. Another two endothermic peaks occur at 125.6 °C, corresponding to the Curie transition of BaTiO<sub>3</sub>, and at 146.23 °C, which corresponds to the melting transition ( $T_m$ ) of the copolymer. In the cooling stage, two exothermic peaks are observed at 132.4 °C and 78.9 °C. These peaks represent the crystallization temperature of the copolymer, represented by  $T_s$ . The thermal behavior of the P(VDF-TrFE)/BaTiO<sub>3</sub> film can be compared to the literature, as seen in Genchi et al. (2016), Vacche et al. (2014) and Vacche et al. (2012) [60,62,63], where similar transition temperatures were found as in this study.

The crystallinity of the composite was analyzed according to the data obtained by thermal events. In this way, it was possible to study the changes in the crystallinity after BaTiO<sub>3</sub> addition, as seen in Table 6.

**Table 6.** Curie temperature ( $T_c$ ), melting temperature ( $T_m$ ), crystallization enthalpy ( $\Delta H_c$ ), melting enthalpy ( $\Delta H_m$ ), and material crystallinity ( $\Delta X_c$ ).

Components	$T_c$ (°C)	$T_m$ (°C)	$\Delta H_c$ (J·g <sup>-1</sup> )	$\Delta H_m$ (J·g <sup>-1</sup> )	$\Delta X_c$ (%)
P(VDF-TrFE)	112.5	146.5	7.59	16.32	36.26
P(VDF-TrFE)/BaTiO <sub>3</sub>	137.5	146.2	6.48	22.07	49.04

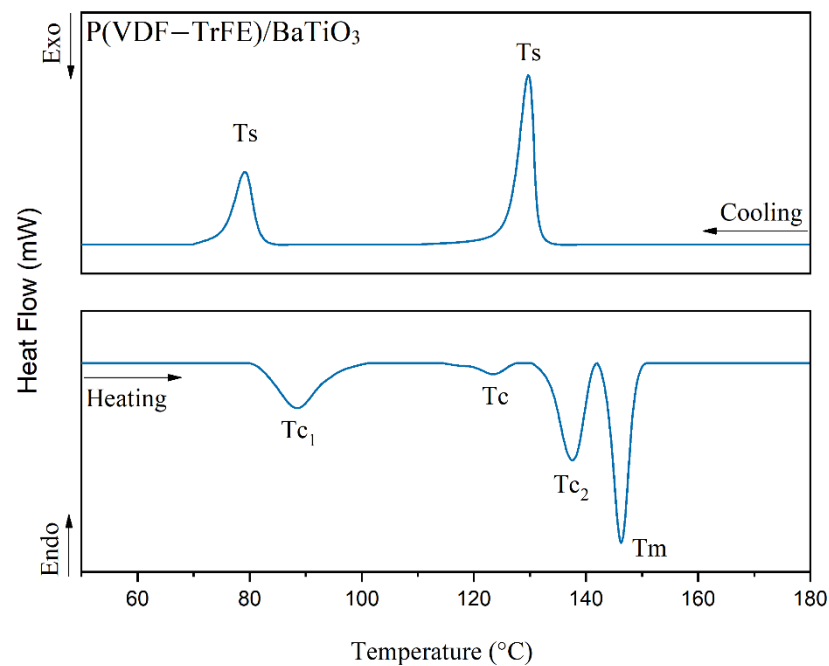
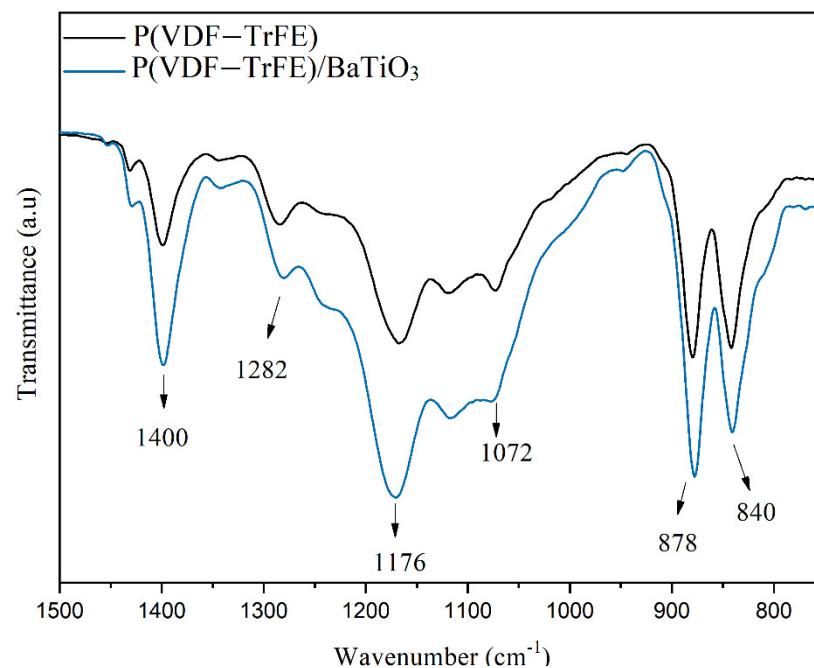


Figure 5. DSC thermogram of P(VDF-TrFE)/BaTiO<sub>3</sub> film at 50 °C to 180 °C.

The crystallinity of the copolymer is in agreement with the literature, as observed in Nunes-Pereira et al. [64]. Genchi et al. [60] discussed the melting enthalpy of the material, which had an increase from  $22 \text{ J}\cdot\text{g}^{-1}$  to  $28 \text{ J}\cdot\text{g}^{-1}$ , thus raising the crystallinity of the copolymer when BaTiO<sub>3</sub> particles were incorporated. However, Vacche et al. [63], reported in their research that the addition of BaTiO<sub>3</sub> did not change the degree of crystallinity of the polymer after its recrystallization. These authors confirmed that at a certain volume of ceramic particles added to the polymer matrix, the crystallinity of the polymer also does not change significantly. In the present study, it can be observed that the addition of ceramic material particles into the polymer matrix increased the crystallinity of the copolymer by 15%, thus confirming the studies of Genchi et al. [60]. The enthalpy of fusion increased approximately from 16 to 22%, meaning that the energy absorbed in the fusion of the compound is higher when related to the fusion energy of the copolymer.

The spectra obtained through the FTIR technique were assigned to the crystalline phases of the P(VDF-TrFE)/BaTiO<sub>3</sub> film. The composite, being a copolymer and ceramic, has a characteristic vibration mode for each phase, which is discriminated through the absorption bands of atomic vibrations. For this reason, the study of the phases of the composite before and after the addition of BaTiO<sub>3</sub> is relevant. Figure 6 shows the FTIR spectra of P(VDF-TrFE) in powder form compared with the FTIR spectra of P(VDF-TrFE)/BaTiO<sub>3</sub>. Intense absorption bands are exhibited at  $840 \text{ cm}^{-1}$ ,  $1282 \text{ cm}^{-1}$ , and  $1400 \text{ cm}^{-1}$ , characteristic of the ferroelectric  $\beta$  phase of P(VDF-TrFE). The peaks from  $1072 \text{ cm}^{-1}$ – $1176 \text{ cm}^{-1}$  are common to the  $\alpha$ ,  $\beta$ , and  $\gamma$  phases. The peaks at  $840$  and  $878 \text{ cm}^{-1}$  are associated with a  $-\text{C}-\text{F}$  symmetric stretch and  $-\text{CF}_2$  bond in-plane rocking deformation, respectively. The peak at  $1282 \text{ cm}^{-1}$  represents the  $-\text{CF}_2$  asymmetric stretch,  $\text{C}-\text{C}$  bond symmetric stretch and  $\text{CCC}$  scissoring vibration. Finally, the peak at  $1400 \text{ cm}^{-1}$  is associated with the  $-\text{CH}_2$  wagging frequency and  $-\text{C}-\text{C}-$  asymmetric stretch [27,65–67]. These peaks suffered an intense increase after the incorporation of BaTiO<sub>3</sub> in the polymeric matrix, which reflects in the piezoelectricity of the material, as seen in Qi et al. (2013) [66]. According to these authors, the increase in the crystallinity of the copolymer after BaTiO<sub>3</sub> addition can be explained by the chemical bonding between them. The BaTiO<sub>3</sub> content increases due to the oxygen vacancies in the composite matrix, which have positive charges. The fluorine atoms of the polymer, which have negative charges, fill the oxygen vacancies. Consequently, the

interface and the space charges are decreased, allowing the electric dipoles to move and rotate easily, increasing the dielectric constant of the composite.



**Figure 6.** FTIR spectra of P(VDF-TrFE) and P(VDF-TrFE)/BaTiO<sub>3</sub> in the wavenumber ranging from 1500 to 800 cm<sup>-1</sup>.

Analyzing the diffractogram in Figure 7a is possible to verify that P(VDF-TrFE) presents crystalline behavior. The P(VDF-TrFE) spectra show a broad peak at 19.9°, which corresponds to the reflection of crystalline planes (110) and (200) of the orthorhombic phase of the copolymer. This phase has a similar crystalline structure to the  $\beta$ -ferroelectric phase of PVDF, also confirmed by the FTIR analysis [68]. Furthermore, a small peak is observed at 17.1° corresponding to the  $\alpha$  phase of P(VDF-TrFE). The copolymer semi-crystalline phase is noted at 18.7°, which is represented by the inflection point in the diffractogram, as observed in Genchi et al. [60]. Figure 7b shows the BaTiO<sub>3</sub> diffractogram. The lattice parameter data obtained show that the unit cell of BaTiO<sub>3</sub> is tetragonal of the crystalline system P4 mm, as observed in the crystallographic sheet PDF-2 05-0626. Complementing the analysis, these results confirm that there are no BaCO<sub>3</sub> impurities in the ceramic powder [68,69]. Ti-30Ta spectrum can be seen in Figure 7c, which corresponds to the crystallographic sheet PDF-2 01-089-5009. The spectrum confirms the presence of the characteristic peaks of the hexagonal metastable phase  $\alpha''$ . These results can be confirmed in previous studies [70–72]. Finally, the spectrum of the composite formed from the Ti-30Ta alloy coated with P(VDF-TrFE)/BaTiO<sub>3</sub> film can be seen in Figure 7d. Analyzing the diffractogram, seen are associated peaks with the phases of all materials. The diffracted peak in the angular region that corresponds to 20° represents the P(VDF-TrFE) copolymer peak. Peaks viewed at 30–35° correspond to the BaTiO<sub>3</sub> tetragonal phase. The  $\alpha''$  phase of the alloy is represented by peaks found at 40°. These peaks suffered a considerable decrease in their relative intensity when compared to the Ti-30Ta alloy diffractogram. This decrease may be related to the P(VDF-TrFE)/BaTiO<sub>3</sub> coating, which interfered in the diffraction of the corresponding plane. Moreover, there were no significant phase changes attributed to the coating process.

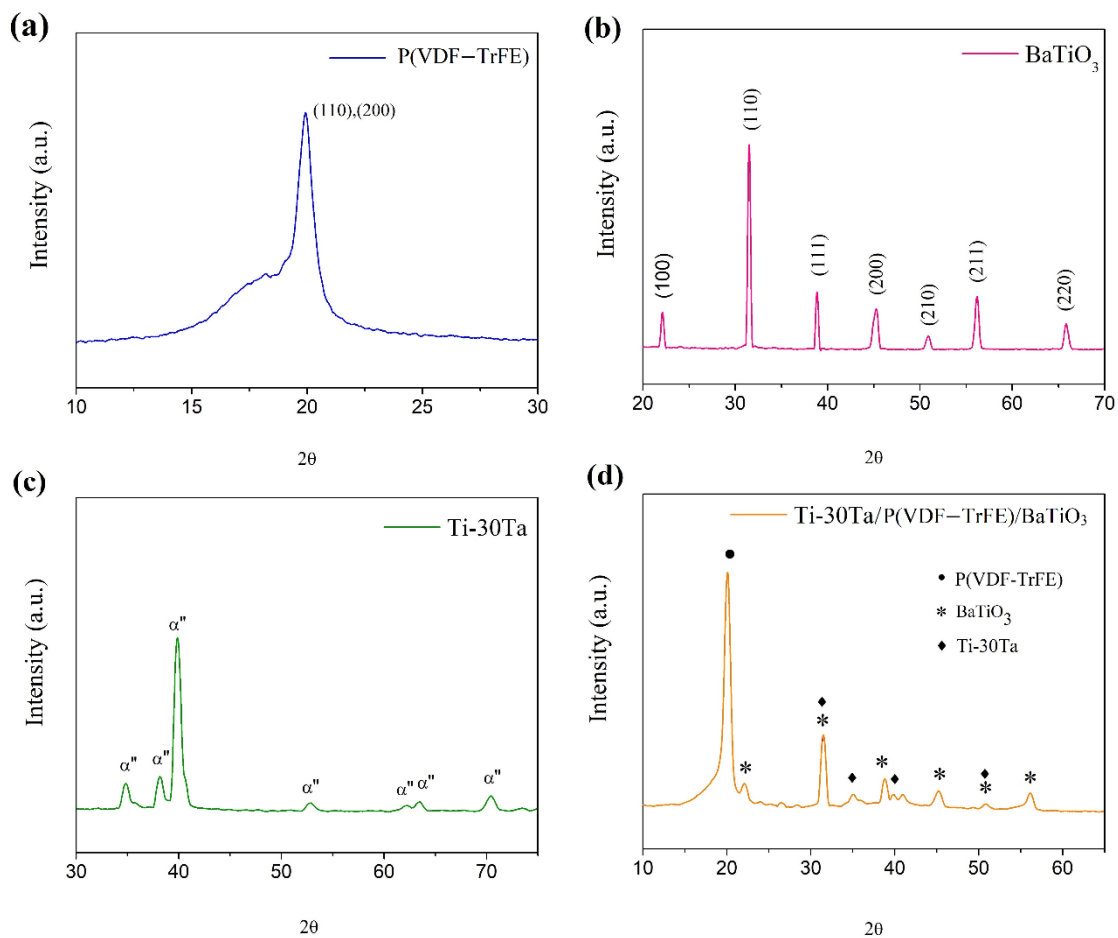


**Figure 7.** Diffractogram of (a) P(VDF-TrFE); (b) BaTiO<sub>3</sub> calcinated at 1380 °C; (c) Ti-30Ta alloy and (d) Ti-30Ta with polished surface treatment coated with P(VDF-TrFE)/BaTiO<sub>3</sub>.

### 3.3. Study of the Deposition Process: Influence of the Temperature on Film Adhesion

To study the temperature influence on the quality of substrate coating, the samples were subjected to three different temperatures during all coating processes for the polish surface treatment, such as the samples with the acid etching treatment. At room temperature, it was found that the film did not adhere to the substrate surface, as seen in Figure 8a. At 100 °C, there was adhesion of the film on the substrate. However, after a time interval, the deposited film could be removed from the substrate, indicating poor adherence, as Figure 8b shows. Figure 8c shows the substrate heated at 150 °C, where the deposited film remained fixed on the surface samples. Furthermore, no defects, wrinkles, or heterogeneities were observed on the coated films. The adhesion of the film can be explained by the increase in temperature, which influences the atoms of the film to interact with the substrate atoms, creating an atomic bonding stronger when compared to the substrate at room temperature [73]. Besides, the rough substrate presents higher thermal resistance after the heating process, increasing the thermal interaction of the substrate with the droplets [74].

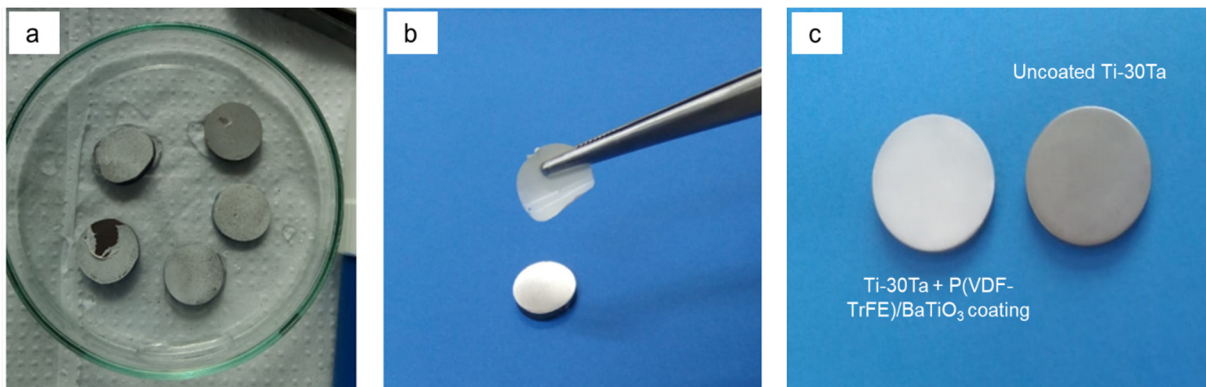


**Figure 8.** Study of temperature influence in the coating process: (a) substrate at room temperature; (b) substrate at 100 °C; (c) substrate at 150 °C.

It is worth pointing out that the film stability is adequate when the material is subjected at temperatures above 150 °C, which is when P(VDF-TrFE) melting occurs, and at temperatures above 450 °C where thermal degradation of the copolymer occurs, as described previously in this study. Thus, the characteristics of the material have not changed due to the thermal treatment of the substrate during the coating process. The temperature rise on the substrate during the coating process also resulted in immediate evaporation of the DMF used in the composite synthesis, which has a boiling point of 153 °C. This fact can be considered an influential factor in film adhesion due to the solidification of the P(VDF-TrFE)/BaTiO<sub>3</sub> film during the coating process.

The dispersion of the BaTiO<sub>3</sub> particles in the polymeric matrix used to coat the Ti-30Ta substrate can be observed in Figure 9. The ceramic particles, represented by white agglomerations, are evenly distributed in the P(VDF-TrFE) film, represented by the dark area in the SEM image. Additionally, the dispersion of the particles in the matrix is homogeneous, confirming that the copolymer and the ceramic have compatible interfaces, as seen in previous studies [15,29,32,57].

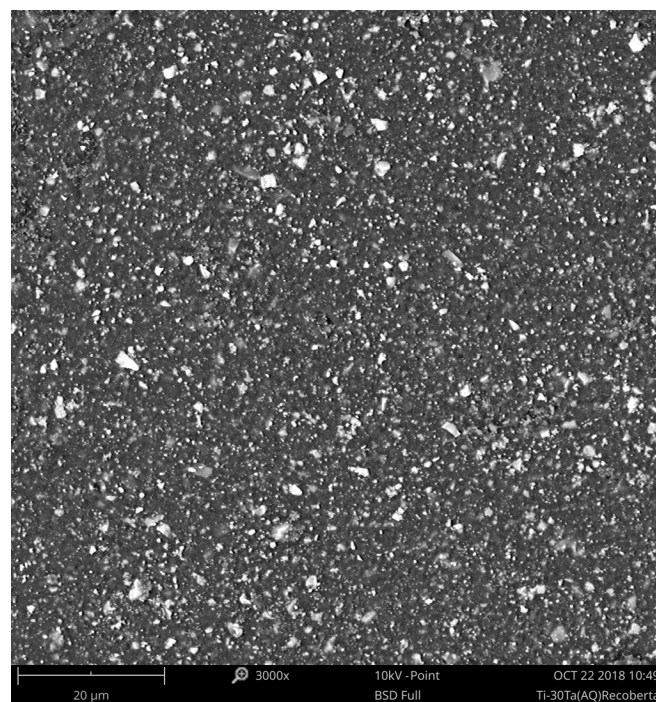


**Figure 9.** SEM of BaTiO<sub>3</sub> dispersion in the P(VDF-TrFE) matrix after the coating process.

The use of the spray as a coating technique forces the solvent to migrate to the water droplets deposited in parallel to the composite, causing the precipitation of the P(VDF-TrFE)/BaTiO<sub>3</sub> on the substrate. For this reason, the composite homogeneity is guaranteed, since the solvent output increases the composite viscosity, stabilizing the BaTiO<sub>3</sub> particles.

### 3.4. Evaluation of the Coated Ti-30Ta Alloy with the P(VDF-TrFE)/BaTiO<sub>3</sub> Film

#### 3.4.1. Scratch Test

Scratch testing provides information about different modes of film failure through the use of a nanoindenter, which moves linearly across the coated sample. The normal force (N) suffers a gradual increase until the first failure occurs. The load that causes this failure is called critical load ( $L_c$ ), and it is considered the main parameter in the evaluation of coating adhesion on the substrate [43,56].

Figure 10a,b represents the behavior of the coating of cp-Ti with polish and acid etching treatment, respectively, and Figure 10c,d represents the behavior of the coating of Ti-30Ta with polish and acid etching treatment when a progressive load is applied.  $L_{c1}$  is the first critical load, characterized by the appearance of initial cracks on the substrate. Increasing the load it is possible to observe a region with a groove followed by small cracks, represented by  $L_{c2}$ . This type of failure is described as a cohesive failure, which is caused by the traction imposed by the indenter as it stresses the thin and fragile film deposited on a ductile substrate [75]. From  $L_{c3}$ , when the critical load is reached, what occurs is the substrate exposition and film fragmentation of considerable length, indicating an adhesive failure. This fragmentation is laterally extended until the end of the scratches made by the indenter. At this point, it is observed that the film forms a wrinkle, indicating that the indenter was tightening the coating until the complete removal of the load.

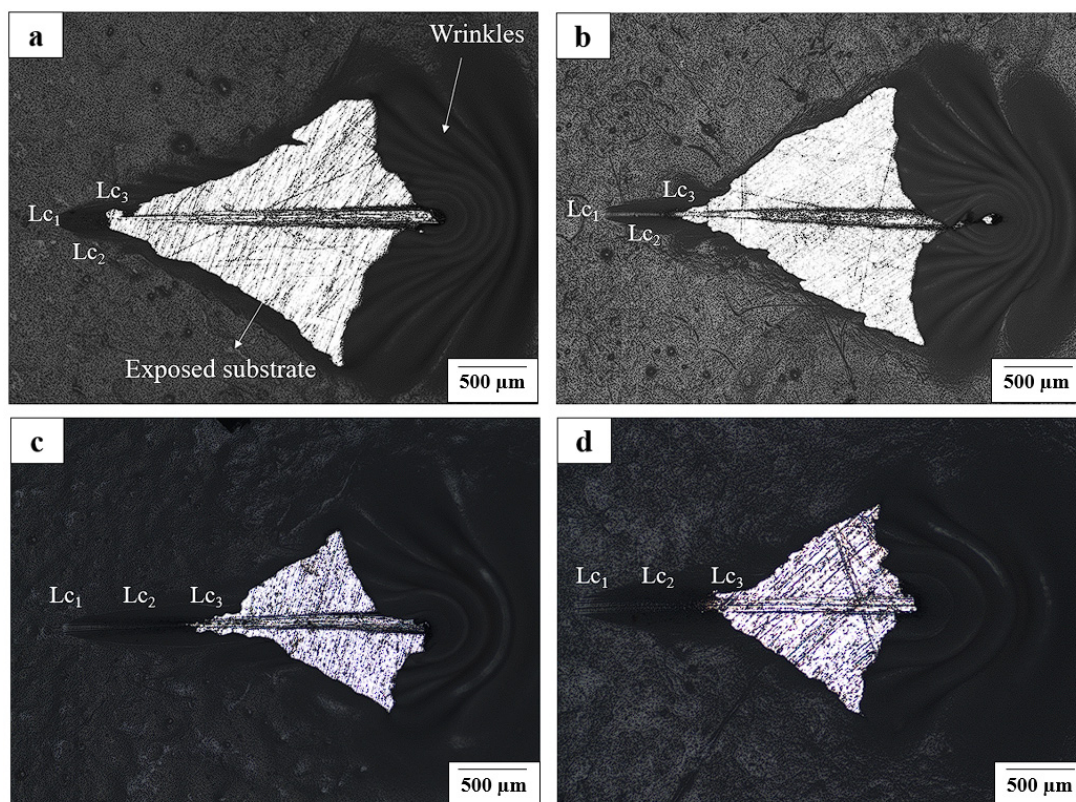


**Figure 10.** Optical microscopy of the scratch tracks performed on the coated surface (a) cp-Ti with polish treatment; (b) cp-Ti with acid etching treatment cp-Ti; (c) Ti-30Ta with polish treatment; (d) Ti-30Ta with acid etching treatment. Ti-30Ta:  $L_{c1}$  represents the first delamination of the coating;  $L_{c2}$  is the transition region of delamination and  $L_{c3}$  is the region where the damage is maximum.

According to Kusakabe et al. [76], the cohesive failure in thin films can be explained due to compression causing wrinkles and storing energy on the surface. When the energy released by the indenter is higher than the free interfacial surface energy between the film and substrate, film delamination and coating failure occur.

The critical load obtained for the polish treatment and acid etching treatment samples is shown in Table 7. The results demonstrate that the critical load associated with the surface treatment of the samples was divergent. For the polished cp-Ti samples, the value found was the lowest, showing poor adhesion compared with the acid etching samples. For the polished Ti-30Ta alloy,  $L_c$  was significantly higher. Thereby, it can be concluded that the film presents better adhesion on Ti-30Ta with the polished surface ( $\approx 9.5$  MPa), since a considerable load was necessary to remove the P(VDF-TrFE)/BaTiO<sub>3</sub> coating when compare to the cp-Ti samples. Although the roughness for the two types of surface treatments present similar values, the morphology of the rough surface is divergent, as shown in Figure 2. As the polished surface presents a surface with peaks and valleys, the total surface area was increased, which can improve the initial adhesion strength due to the film penetrating the grooves, promoting mechanical interlocking. Besides, these results were expected in terms of the surface energy and wettability described previously ( $57.33 \pm 1.35$  mN/m and  $\approx 2^\circ$ , respectively), corroborating the idea that the higher the surface energy and hydrophilicity of the sample surface, the greater the film adhesion on substrate.

**Table 7.** Critical load  $L_c$  obtained via scratch test.

Samples	Critical Load $L_c$ (MPa)	
	Polish	Acid Etching
cp-Ti	$5.23 \pm 0.3$	$6.57 \pm 0.9$
Ti-30Ta	$9.56 \pm 0.8$	$8.36 \pm 0.4$

Comparing these values to the literature, it can be concluded that besides the coating process, the morphology, composition, and crystallinity of the film all influence the adhesion strength. Coatings obtained by plasma spraying presented an adhesion strength of 2–23 Mpa [74]. Coating techniques using electrochemical deposition showed values in a range of 5–15 Mpa [77]. The painting method used for coating Ti substrates with hydroxyapatite presented an adhesion strength of 15–19 Mpa [78]. Some studies reported values on the order of 30–40 Mpa when sanding blasting was used as surface pre-treatment to improve adhesion strength [79].

### 3.4.2. Sectional Study of the Coated Substrate

The interface cross-section between the cp-Ti substrate and film is shown in Figure 11a, where the adhesion seems to occur by the sprinkles of the film on the surface, and in Figure 11b where it can be seen that a fraction of the film peeled off from the surface, indicating weak adhesion of the film on the acid-etched substrate. Figure 11c,d represents a positive result of the Ti-30Ta with both polishing and acid etching treatment coated with P(VDF-TrFE)/BaTiO<sub>3</sub> films. First, the layer of the film deposited on the substrate can be observed and a free-solidification of the composite during the deposition, indicating physical adhesion. This layer is fundamental for the development of the adhesion force, considering the contact between the surface and the coating [80].

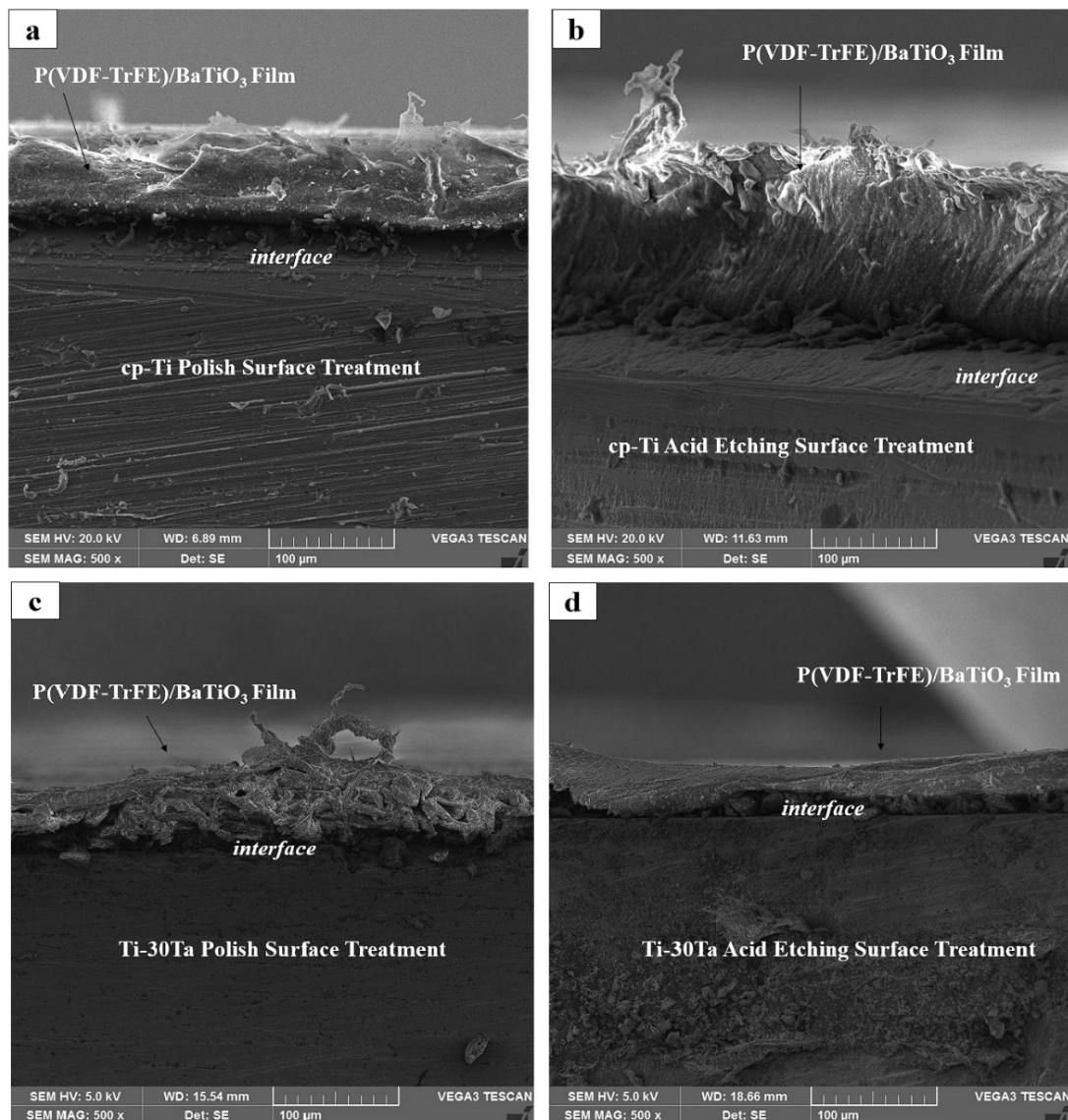


**Figure 11.** (a,b) cp-Ti substrate interface view, showing an adhesive failure; (c,d) Ti-30Ta substrate interface view.

### 3.4.3. Surface Characterization of the Film onto Substrate Surface Energy

The surface properties of an implant, such as the topography and surface energy, improve its wettability characteristics, which influence the osseointegration process due to the interaction of the implant surface and the biological environment [81]. According to Feng et al. [82], the cells behave better when they are in contact with high surface energy, characterized by a rough surface. Besides, cell adhesion on the implant surface is considered excellent when the surface energy of the coating is considered higher than the surface energy of the cell [83].

Table 8 shows the surface energy calculated after the coating process. Analyzing the data, the surface energy for both coated samples is very close due to the contact angle measured relative to the surface of P(VDF-TrFE)/BaTiO<sub>3</sub> film, which is the same for both samples and has the same microstructural and surface characteristics, regardless of the substrate.

**Table 8.** Surface energy of the coated cp-Ti and Ti-3-Ta samples.

Sample	Surface Energy (mN/m)	
	$\gamma_s$	
Ti-30Ta/P(VDF-TrFE)/BaTiO <sub>3</sub>	41.27	
cp-Ti/P(VDF-TrFE)/BaTiO <sub>3</sub>	40.13	

Redey et al. [84] observed that osteoclasts adhesion related to the surface energy on different surfaces. It was found that for materials with a surface energy of 48 mN/m and 58 mN/m there was a higher adherence of cells when compared to the surface with the energy of 9 mN/m. Feng et al. presented good results for osteoblast adhesion on surfaces of 35 mN/m. These surface properties are essential for biomaterials used in dental and orthopedic implants due to the fact that these materials can mimic the natural architecture of the bone, for example.

#### Surface Wettability

Surface wettability is considered the first and most critical property of an implant material considering the initial stage of the biological recovery as a result of an implanted biomaterial. This characteristic allows the control of the protein adsorption, which reflects directly on the implant surface cell anchorage [85]. The wettability of the coated samples is reported in Table 9.

**Table 9.** Wettability of the cp-Ti and Ti-30Ta coated samples.

Samples	Contact Angle $\theta$ (°)	
	Polish	Acid Etching
cp-Ti/P(VDF-TrFE)/BaTiO <sub>3</sub>	78.9 ± 5.8	80.3 ± 5.9
Ti-30Ta/P(VDF-TrFE)/BaTiO <sub>3</sub>	82.9 ± 5.3	85.1 ± 4.2

Analyzing the data, it is observed that both cp-Ti and Ti-30Ta samples presented close contact angles when compared to each other, demonstrating that the type of surface treatment prior to the coating process and the difference in the materials used as a substrate did not interfere with the wettability characteristics of the P(VDF-TrFE)/BaTiO<sub>3</sub> coating. Regarding the nature of the coating material, it was found that the film surface has hydrophilic characteristics, with values less than 90°. It is important to note that the copolymer has a hydrophobic nature due to the electronegativity of the fluorine atoms. The decrease in the contact angle of the P(VDF-TrFE)/BaTiO<sub>3</sub> obtained compared to P(VDF-TrFE) (>90°) can be attributed to the addition of the ceramic in the polymeric matrix, where the C-O and C=O functional groups of the surface of BaTiO<sub>3</sub> interact with the dipoles of PVDF, forming an electroactive  $\beta$ -phase [86]. Additionally, the contact angle measurements showed a low standard deviation when compared with the nominal contact angles observed for the coated samples. These findings suggest the presence of homogeneous films coated on Ti-30Ta substrate.

The wettability of the coated samples through the behavior of deionized water can be seen in Figure 12, where there was a decrease in the contact angle of approximately 15° for each time interval measured. Besides the hydrophilicity, the water spreading can also be attributed to the surface morphology, as the irregular granules with a rough surface of BaTiO<sub>3</sub> dispersed in the polymeric matrix.

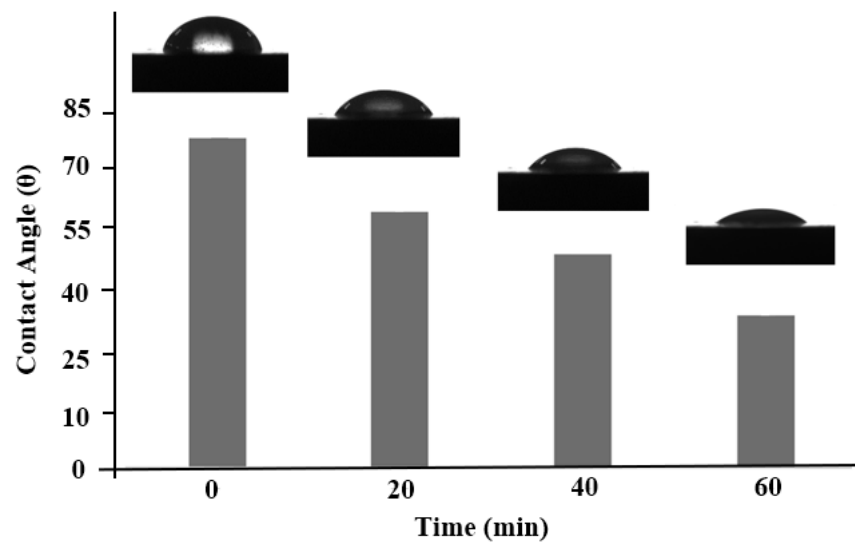


**Figure 12.** Wettability of the P(VDF-TrFE)/BaTiO<sub>3</sub> film through the contact angle.

Furthermore, when a biomaterial is implanted into the human body, the fast protein adsorption acts to connect the external surface with the biological environment, translating the material surface properties and, consequently, influencing cellular differentiation and proliferation. According to Silva-Bermudez and Rodil [50] and Gittens et al. [87], a hydrophilic surface promotes protein adsorption, and a hydrophobic surface, which has low surface energy, inhibits the cellular attachment sites, resulting in poor adhesion of cells [88].

#### Surface Roughness

The presence of roughness on the surface of implants affects the implant-bone connection, promoting an initial stabilization so that bone cells can attach and grow on the implant surface. Thus, the topography with a greater surface area can promote enhanced protein interaction [81]. This property also influences the protein adsorption, as well as induces the conformation and orientation adopted by proteins upon adsorption [89]. However, it has been proved that these surface properties also can influence bacterial adherence to the implants [90]. The roughness of the film deposited on cp-Ti and Ti-30Ta substrates is represented in Table 10, where the obtained data indicate that there is no significant difference between both samples.

**Table 10.** Roughness of the P(VDF-TrFE)/BaTiO<sub>3</sub> deposited on cp-Ti and Ti-30Ta substrates.

Roughness (μm)	
Samples	R <sub>a</sub>
Ti-30Ta/P(VDF-TrFE)/BaTiO <sub>3</sub>	0.254 ± 0.3
cp-Ti/P(VDF-TrFE)/BaTiO <sub>3</sub>	0.240 ± 0.5

## 4. Biological Assays

### 4.1. Evaluation of Biofilm Formation

The presence of pathogenic microorganisms, and the development of biofilms around an implant, are the main causes of body responses, such as infections and inflammation of the recovering tissue [91]. When the material is implanted, the body stimulates a series of biological events, including the interaction between bacteria and host cells, that intend to colonize the implant surface. The bacterial structure has functional groups on its surface, which implies interactions between the bacteria and the ions present on the surface of the implant, damaging the healthy cells of the tissue [92,93]. For this reason, treatment with antibiotics for a long period is required, as well as several surgical procedures, possibly leading to the most serious consequence, the removal of the implant [94].

Biofilm formation occurs when the biological environment offers favorable conditions for the multiplication of bacteria in the implant and adjacent tissue. In particular, bacterial strains surrounding implants have high resistance to antibiotics, such as the Gram-positive *Staphylococcus aureus* and *Staphylococcus epidermidis*, since these types of bacteria have a higher incidence when related to infections associated with implantable medical devices [44,95,96].

The bar chart illustrated in Figure 13 represents the comparison between the two types of bacteria and the adhesive behavior of both, evaluated on P(VDF-TrFE)/BaTiO<sub>3</sub> coating surface and non-coated surface. Statistically, the CFU values (colony-forming unit) for the *S. aureus* did not show significant differences. This means that for both surfaces (i.e., coated and non-coated), the growth of colonies was practically the same, indicating that the P(VDF-TrFE)/BaTiO<sub>3</sub> film did not play a significant role in the formation of biofilms. However, concerning the *S. epidermidis*, the coated samples showed a higher colony formation when compared to *S. aureus*.

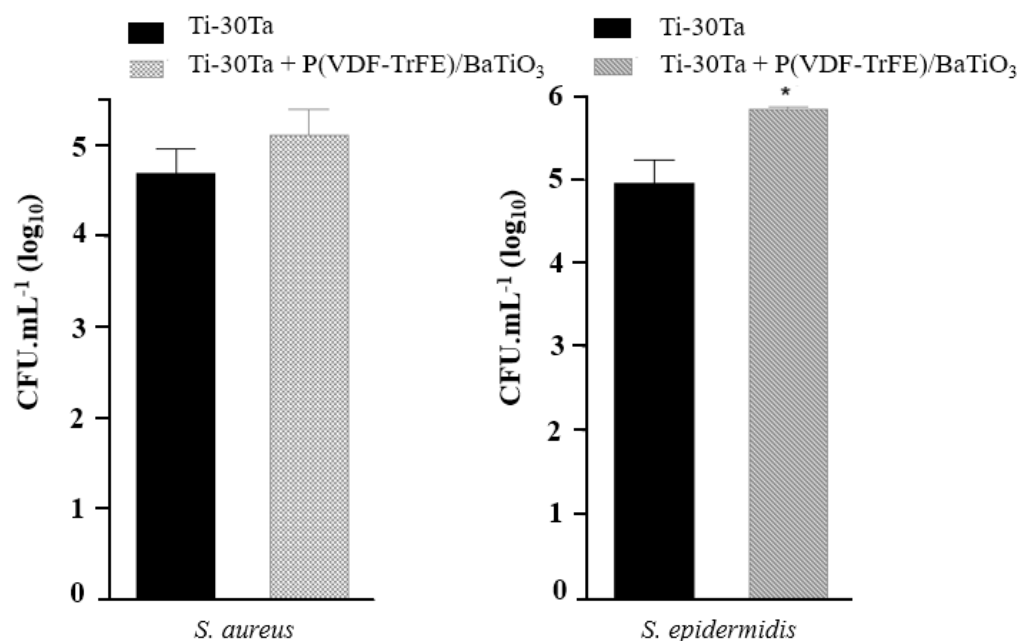


**Figure 13.** Comparative bar chart of colony-forming units (CFU) for *S. aureus* and *S. epidermidis* obtained using Student's *t*-test. \* indicates that the difference between the samples are statistically significant ( $p < 0.05$ ) when compared to the non-coated and coated samples for *S. epidermidis*.

In contrast to the *S. aureus*, which may be repulsed by the chemical surface properties of some polymers, the *S. epidermidis* has a high ability to promote its surface adhesion even in polymeric coatings, which can be explained by the nonprotein adhesins used by them to adhere to the coated surface [97,98]. Besides, according to Wu et al. [99], the *S. epidermidis* prefers to colonize rough surfaces with high contact areas, characterized by the depressions and grooves on the surface. Damiati et al. [89] and Lee et al. [100] indicated an ideal value for surface roughness below 0.2  $\mu\text{m}$ , which bacterial adhesion can be reduced significantly. Comparing this value with the roughness obtained in this work, which corresponds to  $0.254 \pm 0.05 \mu\text{m}$ , the roughness of the film may have influenced the biofilm colonization since the surface presents a suitable topography for bacterial growth.

Besides, the *S. epidermidis* is a hydrophobic bacteria and is able to bond to the surface with van der Waals interaction and, according to Cerca et al. [101], the hydrophobic interactions are stronger than other covalent forces, promoting a strong adhesion on the surface [102,103]. Considering the results of this study, even though the surface is characterized as hydrophilic, the contact angle is still high ( $\theta \approx 85^\circ$ —near the limit of contact angle for hydrophobic surfaces), which may imply that the material affects the initial adhesion of

the bacteria. On the other hand, the adhesion of the *S. aureus* was reduced due to this strain choosing hydrophilic surfaces, characterized by lower contact angles.

The distribution of the biofilms on the non-coated and coated Ti-30Ta can be seen in Figure 14. Figure 14a shows that the *S. aureus* formed agglomerated structures in the grooves of the polish-treated Ti-30Ta surface. Figure 14b represents the *S. aureus* biofilm formation on the coated sample. Besides, the agglomeration can also be seen in the groove of the coated surface. According to Cuello et al. [104] and Yang et al. [105], *S. epidermidis*, *P. aeruginosa*, and *S. aureus* choose to adhere to surfaces with a large groove, which implies a higher contact area. The beads dispersed on the surface can be explained by the drops from the process of spray coating, and these irregularities can influence the biofilm formation. *S. epidermidis* adhesion is seen in Figure 14c,d, which represents the biofilm adhesion on non-coated Ti-30Ta and coated Ti-30Ta surfaces, respectively.

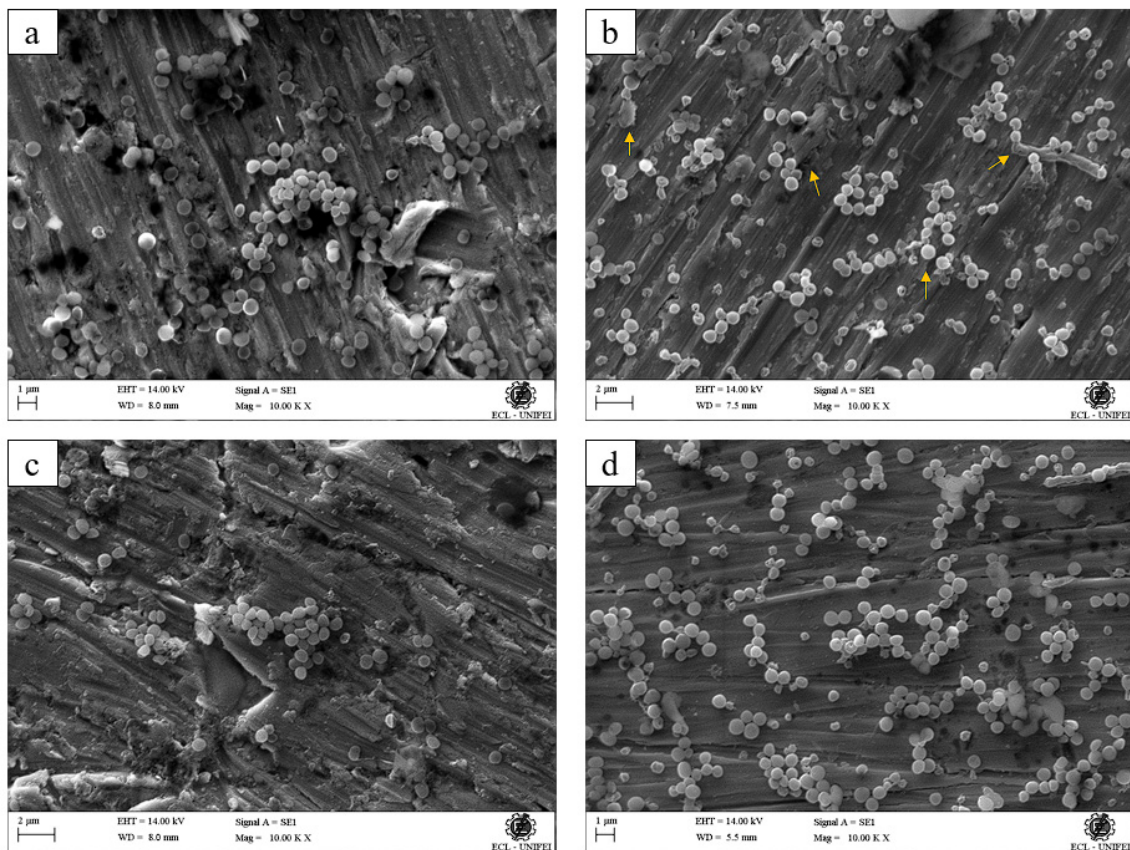


**Figure 14.** Biofilm distribution on the non-coated and coated Ti-30Ta. (a) *S. aureus* biofilm on Ti-30Ta polished surface. (b) *S. aureus* biofilm on Ti-30Ta coated with the piezoelectric film. The beads on the surface, represented by the yellow arrow, may influence the biofilm formation. (c) *S. epidermidis* biofilm formation on Ti-30Ta polished surface. (d) *S. epidermidis* biofilm growth on the Ti-30Ta coated sample. In all SEM images, we can observe that the bacteria growth occurs in the grooves, following a preferential direction.

#### 4.2. Hemocompatibility Test

The rate of hemolysis of the Ti-30Ta alloy and the Ti-30Ta alloy coated with P(VDF-TrFE)/BaTiO<sub>3</sub> film can be seen in Figure 15. The results obtained for both samples are below the hemolysis rate (<5%) and, statistically, there are no significant differences between them, thus indicating no hemolytic activity. This test shows that the Ti-30 Ta alloy and the coated alloy do not present hemolytic activity, thus these surfaces are characterized as hemocompatible.

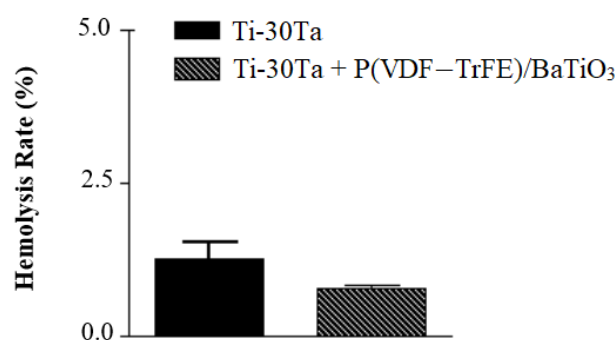


**Figure 15.** Hemolysis rate of Ti-30Ta alloy without the coating process and after coating process with  $p < 0.05$ . Both surfaces do not present hemolytic activity indicating they are hemocompatible.

## 5. Conclusions

The proposed coating process methodology proved to be effective, showing that the deposition of P(VDF-TrFE)/BaTiO<sub>3</sub> on Ti-based substrates was homogeneously distributed on the surface. In addition, the spray coating technique applied in this study is low cost and straightforward when compared with other coating processes, such as plasma spray. The adhesive bond test result of the coating was superior in samples with a polish treatment, with a critical load responsible for coating failure of approximately 10 Mpa. The biofilm assay showed that the growth of *Staphylococcus epidermidis* was higher when compared to *Staphylococcus aureus* on the piezoelectric film. The hemolysis assay confirms that the material has high hemocompatibility. According to physicochemical results, the Ti-30Ta coated with P(VDF-TrFE)/BaTiO<sub>3</sub> film has potential when related to piezoelectric properties associated with the  $\beta$  phase, since the piezoelectricity is intrinsically connected to this phase. However, the authors suggest that in vitro and in vivo analyses should be made to confirm the potential of the coated alloy to stimulate the growth and differentiation of the cells from bone tissue, for example. Another suggestion is to associate the biofilm formation with the poled surface, considering that the piezoelectric stimulus can provide an antibacterial effect.

**Author Contributions:** Conceptualization, R.G.; methodology, L.M.S.R., L.A.C.d.R.S. and M.E.-S.; validation, L.M.S.R., T.A.N.R. and V.C.T.; formal analysis, L.M.S.R.; investigation, L.M.S.R.; resources, D.S.; data curation, R.G.; writing—original draft preparation, L.M.S.R.; writing—review and editing B.H.B.K., L.V.B.V.F., P.C. and S.E.S.; supervision and editing, R.G.; project administration, R.G.; funding acquisition, D.S., P.C. and A.P.R.A.C. All authors have read and agreed to the published version of the manuscript.

**Funding:** This research received no external funding.

**Data Availability Statement:** Data presented in this article are available at request from the corresponding author.

**Acknowledgments:** The authors would like to thank the CAPES (Coordination of Superior Level Staff Improvement) for the financial support, CNPq (National Council for Scientific and Technological Development), FAPEMIG (Foundation for Research Support of State of Minas Gerais), FAPESP (Foundation for Research Support of State of São Paulo) and all other agencies from the Brazilian government.

**Conflicts of Interest:** The authors announce no potential conflict of interest concerning the research, authorship, or publication of this article.

## References

1. Civantos, A.; Martínez-Campos, E.; Ramos, V.; Elvira, C.; Gallardo, A.; Abarrategi, A. Titanium Coatings and Surface Modifications: Toward Clinically Useful Bioactive Implants. *ACS Biomater. Sci. Eng.* **2017**, *3*, 1245–1261. [[CrossRef](#)] [[PubMed](#)]
2. Sowa, M.; Simka, W. Electrochemical Behavior of Plasma Electrolytically Oxidized Niobium in Simulated Physiological Environment. *Surf. Coatings Technol.* **2018**, *344*, 121–131. [[CrossRef](#)]

3. Sarraf, M.; Rezvani Ghomi, E.; Alipour, S.; Ramakrishna, S.; Liana Sukiman, N. A State-of-the-Art Review of the Fabrication and Characteristics of Titanium and Its Alloys for Biomedical Applications. *Bio-Des. Manuf.* **2022**, *5*, 371–395. [[CrossRef](#)] [[PubMed](#)]
4. İzmir, M.; Ercan, B. Anodization of Titanium Alloys for Orthopedic Applications. *Front. Chem. Sci. Eng.* **2019**, *13*, 28–45. [[CrossRef](#)]
5. Chen, W.; Xu, K.; Tao, B.; Dai, L.; Yu, Y.; Mu, C.; Shen, X.; Hu, Y.; He, Y.; Cai, K. Multilayered Coating of Titanium Implants Promotes Coupled Osteogenesis and Angiogenesis in Vitro and in Vivo. *Acta Biomater.* **2018**, *74*, 489–504. [[CrossRef](#)]
6. Sidambe, A.T. Biocompatibility of Advanced Manufactured Titanium Implants—A Review. *Materials* **2014**, *7*, 8168–8188. [[CrossRef](#)]
7. Hanawa, T. Titanium-Tissue Interface Reaction and Its Control with Surface Treatment. *Front. Bioeng. Biotechnol.* **2019**, *7*, 170. [[CrossRef](#)]
8. Capellato, P.; Riedel, N.A.; Williams, J.D.; Machado, J.P.B.; Papat, K.C.; Alves Claro, A.P.R. Surface Modification on Ti-30Ta Alloy for Biomedical Application. *Engineering* **2013**, *5*, 707–713. [[CrossRef](#)]
9. Zhou, Y.L.; Niinomi, M.; Akahori, T. Effects of Ta Content on Young's Modulus and Tensile Properties of Binary Ti-Ta Alloys for Biomedical Applications. *Mater. Sci. Eng. A* **2004**, *371*, 283–290. [[CrossRef](#)]
10. Ibrahim, M.K.; Hamzah, E.; Saud, S.N.; Nazim, E.M.; Iqbal, N.; Bahador, A. Effect of Sn Additions on the Microstructure, Mechanical Properties, Corrosion and Bioactivity Behaviour of Biomedical Ti-Ta Shape Memory Alloys. *J. Therm. Anal. Calorim.* **2018**, *131*, 1165–1175. [[CrossRef](#)]
11. Chen, Q.; Thouas, G.A. Metallic Implant Biomaterials. *Mater. Sci. Eng. R Rep.* **2015**, *87*, 1–57. [[CrossRef](#)]
12. Schildhauer, T.A.; Robie, B.; Muhr, G.; Köller, M. Bacterial Adherence to Tantalum versus Commonly Used Orthopedic Metallic Implant Materials. *J. Orthop. Trauma* **2006**, *20*, 476–484. [[CrossRef](#)] [[PubMed](#)]
13. Zhu, Y.; Gu, Y.; Qiao, S.; Zhou, L.; Shi, J.; Lai, H. Bacterial and Mammalian Cells Adhesion to Tantalum-Decorated Micro-/Nano-Structured Titanium. *J. Biomed. Mater. Res. Part A* **2017**, *105*, 871–878. [[CrossRef](#)] [[PubMed](#)]
14. Wang, X.; Ning, B.; Pei, X. Tantalum and Its Derivatives in Orthopedic and Dental Implants: Osteogenesis and Antibacterial Properties. *Colloids Surf. B Biointerfaces* **2021**, *208*, 112055. [[CrossRef](#)] [[PubMed](#)]
15. Alhalawani, A.M.; Mehrvar, C.; Stone, W.; Waldman, S.D.; Towler, M.R. A Novel Tantalum-Containing Bioglass. Part II. Development of a Bioadhesive for Sternal Fixation and Repair. *Mater. Sci. Eng. C* **2017**, *71*, 401–411. [[CrossRef](#)] [[PubMed](#)]
16. Harrison, P.L.; Harrison, T.; Stockley, I.; Smith, T.J. Does Tantalum Exhibit Any Intrinsic Antimicrobial or Antibiofilm Properties? *Bone Jt. J.* **2017**, *99*, 1153–1156. [[CrossRef](#)] [[PubMed](#)]
17. Tokarski, A.T.; Novack, T.A.; Parvizi, J. Is Tantalum Protective against Infection in Revision Total Hip Arthroplasty? *Bone Jt. J.* **2015**, *97*, 45–49. [[CrossRef](#)]
18. Mani, G.; Porter, D.; Grove, K.; Collins, S.; Ornberg, A.; Shulfer, R. A Comprehensive Review of Biological and Materials Properties of Tantalum and Its Alloys. *J. Biomed. Mater. Res. Part A* **2022**, *110*, 1291–1306. [[CrossRef](#)]
19. Ching, H.A.; Choudhury, D.; Nine, M.J.; Abu Osman, N.A. Effects of Surface Coating on Reducing Friction and Wear of Orthopaedic Implants. *Sci. Technol. Adv. Mater.* **2014**, *15*, 014402. [[CrossRef](#)]
20. Moore, B.; Asadi, E.; Lewis, G. Deposition Methods for Microstructured and Nanostructured Coatings on Metallic Bone Implants: A Review. *Adv. Mater. Sci. Eng.* **2017**, *2017*, 5812907. [[CrossRef](#)]
21. Uwais, Z.A.; Hussein, M.A.; Samad, M.A.; Al-Aqeeli, N. Surface Modification of Metallic Biomaterials for Better Tribological Properties: A Review. *Arab. J. Sci. Eng.* **2017**, *42*, 4493–4512. [[CrossRef](#)]
22. Pires, A.L.R.; Bierhalz, A.C.K.; Moraes, Á.M. Biomaterials: Types, Applications, and Market. *Quim. Nova* **2015**, *38*, 957–971. [[CrossRef](#)]
23. Kligman, S.; Ren, Z.; Chung, C.H.; Perillo, M.A.; Chang, Y.C.; Koo, H.; Zheng, Z.; Li, C. The Impact of Dental Implant Surface Modifications on Osseointegration and Biofilm Formation. *J. Clin. Med.* **2021**, *10*, 1641. [[CrossRef](#)] [[PubMed](#)]
24. Poon, K.K.; Schafföner, S.; Einarsrud, M.A.; Glaum, J. Barium Titanate-Based Bilayer Functional Coatings on Ti Alloy Biomedical Implants. *J. Eur. Ceram. Soc.* **2021**, *41*, 2918–2922. [[CrossRef](#)]
25. Gnedenkov, S.V.; Sinebryukhov, S.L.; Zavidnaya, A.G.; Egorkin, V.S.; Puz', A.V.; Mashtalyar, D.V.; Sergienko, V.I.; Yerokhin, A.L.; Matthews, A. Composite Hydroxyapatite-PTFE Coatings on Mg-Mn-Ce Alloy for Resorbable Implant Applications via a Plasma Electrolytic Oxidation-Based Route. *J. Taiwan Inst. Chem. Eng.* **2014**, *45*, 3104–3109. [[CrossRef](#)]
26. Magueta, A.F.; Fernandes, M.H.V.; Hortigüela, M.J.; Otero-Irurueta, G.; Vilarinho, P.M. Poly (L-Lactic Acid) Coatings on 316 SS Substrates for Biomedical Devices: The Impact of Surface Silanization. *Prog. Org. Coatings* **2021**, *157*, 106289. [[CrossRef](#)]
27. Bolbasov, E.N.; Popkov, A.V.; Popkov, D.A.; Gorbach, E.N.; Khlusov, I.A.; Golovkin, A.S.; Sinev, A.; Bouznic, V.M.; Tverdokhlebov, S.I.; Anissimov, Y.G. Osteoinductive Composite Coatings for Flexible Intramedullary Nails. *Mater. Sci. Eng. C* **2017**, *75*, 207–220. [[CrossRef](#)]
28. Lopes, H.B.; Santos, T.D.S.; De Oliveira, F.S.; Freitas, G.P.; De Almeida, A.L.; Gimenes, R.; Rosa, A.L.; Beloti, M.M. Poly(Vinylidene-Trifluoroethylene)/Barium Titanate Composite for in Vivo Support of Bone Formation. *J. Biomater. Appl.* **2014**, *29*, 104–112. [[CrossRef](#)]
29. Li, Y.; Liao, C.; Tjong, S.C. Electrospun Polyvinylidene Fluoride-Based Fibrous Scaffolds with Piezoelectric Characteristics for Bone and Neural Tissue Engineering. *Nanomaterials* **2019**, *9*, 952. [[CrossRef](#)]

30. Gimenes, R.; Zaghete, M.A.; Bertolini, M.; Varela, J.A.; Coelho, L.O.; Silva, N.F., Jr. Composites PVDF-TrFE/BT Used as Bioactive Membranes for Enhancing Bone Regeneration. In *Smart Structures and Materials 2004: Electroactive Polymer Actuators and Devices (EAPAD)*; Spie-Int Soc Optical Engineering: Bellingham, WA, USA, 2004; Volume 5385, pp. 539–547. [[CrossRef](#)]
31. Luo, H.; Chen, S.; Liu, L.; Zhou, X.; Ma, C.; Liu, W.; Zhang, D. Core-Shell Nanostructure Design in Polymer Nanocomposite Capacitors for Energy Storage Applications. *ACS Sustain. Chem. Eng.* **2019**, *7*, 3145–3153. [[CrossRef](#)]
32. Lopes, H.B.; de Santana Santos, T.; Freitas, G.P.; de Oliveira, F.; Gimenes, R.; Luiz Rosa, A.; Mateus Beloti, M. Gene Expression Analysis of Bone Tissue Grown on P(VDF-TrFE)/BT Membrane Implanted in Rat Calvarial Defects. *J. Oral Maxillofac. Surg.* **2013**, *71*, e88–e89. [[CrossRef](#)]
33. Scalize, P.H.; Bombonato-Prado, K.F.; de Sousa, L.G.; Rosa, A.L.; Beloti, M.M.; Semprini, M.; Gimenes, R.; de Almeida, A.L.G.; de Oliveira, F.S.; Hallak Regalo, S.C.; et al. Poly(Vinylidene Fluoride-Trifluorethylene)/Barium Titanate Membrane Promotes de Novo Bone Formation and May Modulate Gene Expression in Osteoporotic Rat Model. *J. Mater. Sci. Mater. Med.* **2016**, *27*, 180. [[CrossRef](#)] [[PubMed](#)]
34. Gimenes, R.; Zaghete, M.A.; Espanhol, M.; Sachs, D.; Silva, M.R.A. Promotion of Bone Repair of Rabbit Tibia Defects Induced by Scaffolds of P(VDF-TrFE)/BaTiO<sub>3</sub> Composites. *Bull. Mater. Sci.* **2019**, *42*, 235. [[CrossRef](#)]
35. Capellato, P.; Escada, A.L.A.; Popat, K.C.; Claro, A.P.R.A. Interaction between Mesenchymal Stem Cells and Ti-30Ta Alloy after Surface Treatment. *J. Biomed. Mater. Res. Part A* **2014**, *102*, 2147–2156. [[CrossRef](#)]
36. Owens, D.K.; Wendt, R.C. Estimation of the Surface Free Energy of Polymers. *J. Appl. Polym. Sci.* **1969**, *13*, 1741–1747. [[CrossRef](#)]
37. Xu, L.; Zhang, K.; Wu, C.; Lei, X.; Ding, J.; Shi, X.; Liu, C. Micro-Arc Oxidation Enhances the Blood Compatibility of Ultrafine-Grained Pure Titanium. *Materials* **2017**, *10*, 1446. [[CrossRef](#)]
38. Żenkiewicz, M. Methods for the Calculation of Surface Free Energy of Solids. *J. Achiev. Mater. Manuf. Eng.* **2007**, *24*, 137–145.
39. He, Z.; Rault, F.; Lewandowski, M.; Mohsenzadeh, E.; Salaün, F. Electrospun PVDF Nanofibers for Piezoelectric Applications: A Review of the Influence of Electrospinning Parameters on the  $\beta$  Phase and Crystallinity Enhancement. *Polymers* **2021**, *13*, 174. [[CrossRef](#)]
40. Jiang, J.; Tu, S.; Fu, R.; Li, J.; Hu, F.; Yan, B.; Gu, Y.; Chen, S. Flexible Piezoelectric Pressure Tactile Sensor Based on Electrospun BaTiO<sub>3</sub>/Poly(Vinylidene Fluoride) Nanocomposite Membrane. *ACS Appl. Mater. Interfaces* **2020**, *12*, 33989–33998. [[CrossRef](#)]
41. ASTM D7027; Standard Test Method for Evaluation of Scratch Resistance of Polymeric Coatings and Plastics Using an Instrumented Scratch Machine. ASTM International: West Conshohocken, PA, USA, 2013; Volume 5, pp. 1–9. [[CrossRef](#)]
42. Da Silva, W.M.; Costa, H.L.; De Mello, J.D.B. Transitions in Abrasive Wear Mechanisms: Effect of the Superimposition of Interactions. *Wear* **2011**, *271*, 977–986. [[CrossRef](#)]
43. Teles, V.C.; de Mello, J.D.B.; da Silva, W.M. Abrasive Wear of Multilayered/Gradient CrAlSiN PVD Coatings: Effect of Interface Roughness and of Superficial Flaws. *Wear* **2017**, *376–377*, 1691–1701. [[CrossRef](#)]
44. De Breij, A.; Riool, M.; Kwakman, P.H.S.; De Boer, L.; Cordfunke, R.A.; Drijfhout, J.W.; Cohen, O.; Emanuel, N.; Zaat, S.A.J.; Nibbering, P.H.; et al. Prevention of Staphylococcus Aureus Biomaterial-Associated Infections Using a Polymer-Lipid Coating Containing the Antimicrobial Peptide OP-145. *J. Control. Release* **2016**, *222*, 1–8. [[CrossRef](#)] [[PubMed](#)]
45. Zheng, Y.; Li, J.; Liu, X.; Sun, J. Antimicrobial and Osteogenic Effect of Ag-Implanted Titanium with a Nanostructured Surface. *Int. J. Nanomed.* **2012**, *7*, 875–884. [[CrossRef](#)]
46. ASTM F 756-17; Standard Practice for Assessment of Hemolytic Properties of Materials. ASTM International: West Conshohocken, PA, USA, 2017; Volume 5. [[CrossRef](#)]
47. Liu, H.; Pan, C.; Zhou, S.; Li, J.; Huang, N.; Dong, L. Improving Hemocompatibility and Accelerating Endothelialization of Vascular Stents by a Copper-Titanium Film. *Mater. Sci. Eng. C* **2016**, *69*, 1175–1182. [[CrossRef](#)] [[PubMed](#)]
48. Choi, A.H.; Akyol, S.; Bendavid, A.; Ben-Nissan, B. Nanobioceramic Thin Films: Surface Modifications and Cellular Responses on Titanium Implants. In *Titanium in Medical and Dental Applications*; Woodhead Publishing: Sawston, UK, 2018; pp. 147–173. [[CrossRef](#)]
49. Kendall, K. *Molecular Adhesion and Its Applications: The Sticky Universe*, 1st ed.; Kluwer Academic/Plenum Publishers: Loughborough, UK, 2004; ISBN 0306484064.
50. Silva-Bermudez, P.; Rodil, S.E. An Overview of Protein Adsorption on Metal Oxide Coatings for Biomedical Implants. *Surf. Coatings Technol.* **2013**, *233*, 147–158. [[CrossRef](#)]
51. Biasetto, L.; Elsayed, H. Sphene Silicate Ceramic Coatings on CpTi Substrates: Process Upgrade. *Surf. Coatings Technol.* **2017**, *321*, 416–424. [[CrossRef](#)]
52. Geng, Z.; Wang, R.; Zhuo, X.; Li, Z.; Huang, Y.; Ma, L.; Cui, Z.; Zhu, S.; Liang, Y.; Liu, Y.; et al. Incorporation of Silver and Strontium in Hydroxyapatite Coating on Titanium Surface for Enhanced Antibacterial and Biological Properties. *Mater. Sci. Eng. C* **2017**, *71*, 852–861. [[CrossRef](#)]
53. Zhou, C.; Lei, F.; Chodosh, J.; Paschalis, E.I. The Role of Titanium Surface Microtopography on Adhesion, Proliferation, Transformation, and Matrix Deposition of Corneal Cells. *Investig. Ophthalmol. Vis. Sci.* **2016**, *57*, 1927–1938. [[CrossRef](#)]
54. Guo, L.; Chen, X.; Liu, X.; Feng, W.; Li, B.; Lin, C.; Tao, X.; Qiang, Y. Surface Modifications and Nano-Composite Coatings to Improve the Bonding Strength of Titanium-Porcelain. *Mater. Sci. Eng. C* **2016**, *61*, 143–148. [[CrossRef](#)]
55. Cordeiro, J.M.; Nagay, B.E.; Ribeiro, A.L.R.; da Cruz, N.C.; Rangel, E.C.; Fais, L.M.G.; Vaz, L.G.; Barão, V.A.R. Functionalization of an Experimental Ti-Nb-Zr-Ta Alloy with a Biomimetic Coating Produced by Plasma Electrolytic Oxidation. *J. Alloys Compd.* **2019**, *770*, 1038–1048. [[CrossRef](#)]

56. C1624-05; Standard Test Method for Adhesion Strength and Mechanical Failure Modes of Ceramic Coatings by Quantitative Single Point Scratch Testing. ASTM International: West Conshohocken, PA, USA, 2015; Volume 5, pp. 1–29. [[CrossRef](#)]
57. Packham, D.E. Surface Energy, Surface Topography and Adhesion. *Int. J. Adhes. Adhes.* **2003**, *23*, 437–448. [[CrossRef](#)]
58. Wen, C.; Nouri, A. *Surface Coating and Modification of Metallic Biomaterials*, 1st ed.; Wen, C., Ed.; Woodhead Publishing Limited: Cambridge, UK, 2015; ISBN 9781782423164.
59. Bae, J.H.; Han, M.G.; Chang, S.H. Shear-Deformed Fabric Sensor Made of P(VDF-TrFE) for Damage Detection of Draped Composite Structures: A Feasibility Study. *Compos. Part A Appl. Sci. Manuf.* **2018**, *113*, 242–253. [[CrossRef](#)]
60. Genchi, G.G.; Ceseracciu, L.; Marino, A.; Labardi, M.; Marras, S.; Pignatelli, F.; Bruschini, L.; Mattoli, V.; Ciofani, G. P(VDF-TrFE)/BaTiO<sub>3</sub> Nanoparticle Composite Films Mediate Piezoelectric Stimulation and Promote Differentiation of SH-SY5Y Neuroblastoma Cells. *Adv. Healthc. Mater.* **2016**, *5*, 1808–1820. [[CrossRef](#)] [[PubMed](#)]
61. Simoes, R.D.; Rodriguez-Perez, M.A.; De Saja, J.A.; Constantino, C.J.L. Thermomechanical Characterization of PVDF and P(VDF-TrFE) Blends Containing Corn Starch and Natural Rubber. *J. Therm. Anal. Calorim.* **2010**, *99*, 621–629. [[CrossRef](#)]
62. Vacche, S.D.; Oliveira, F.; Letierrier, Y.; Michaud, V.; Damjanovic, D.; Månson, J.-A.E. Effect of Silane Coupling Agent on the Morphology, Structure, and Properties of Poly(Vinylidene Fluoride–Trifluoroethylene)/BaTiO<sub>3</sub> Composites. *J. Mater. Sci.* **2014**, *49*, 4552–4564. [[CrossRef](#)]
63. Vacche, S.D.; Oliveira, F.; Letierrier, Y.; Michaud, V.; Damjanovic, D.; Månson, J.A.E. The Effect of Processing Conditions on the Morphology, Thermomechanical, Dielectric, and Piezoelectric Properties of P(VDF-TrFE)/BaTiO<sub>3</sub> Composites. *J. Mater. Sci.* **2012**, *47*, 4763–4774. [[CrossRef](#)]
64. Nunes-Pereira, J.; Ribeiro, S.; Ribeiro, C.; Gombek, C.J.; Gama, F.M.; Gomes, A.C.; Patterson, D.A.; Lanceros-Méndez, S. Poly(Vinylidene Fluoride) and Copolymers as Porous Membranes for Tissue Engineering Applications. *Polym. Test.* **2015**, *44*, 234–241. [[CrossRef](#)]
65. Ryu, J.; No, K.; Kim, Y.; Park, E.; Hong, S. Synthesis and Application of Ferroelectric Poly(Vinylidene Fluoride–Co-Trifluoroethylene) Films Using Electrophoretic Deposition. *Sci. Rep.* **2016**, *6*, 36176. [[CrossRef](#)]
66. Qi, Y.; Pan, L.; Ma, L.; Liao, P.; Ge, J.; Zhang, D.; Zheng, Q.; Yu, B.; Tang, Y.; Sun, D. Investigation on FT-IR Spectra and Dielectric Property of PVDF/Inorganic Composites. *J. Mater. Sci. Mater. Electron.* **2013**, *24*, 1446–1450. [[CrossRef](#)]
67. Barkoula, N.M.; Alcock, B.; Cabrera, N.O.; Peijs, T. Fatigue Properties of Highly Oriented Polypropylene Tapes and All-Polypropylene Composites. *Polym. Polym. Compos.* **2008**, *16*, 101–113. [[CrossRef](#)]
68. Cerconi, C.; González-Borrero, P.P. Preparação e Caracterização de Pós e Filmes Finos de BaTiO<sub>3</sub> Sintetizados via Método Pechini. *Rev. Mater.* **2013**, *18*, 1510–1524. [[CrossRef](#)]
69. Wang, S.; Qu, P.; Li, C.; Liu, X. Hydrothermal Synthesis of Dendritic BaTiO<sub>3</sub> Ceramic Powders and Its Application in BaTiO<sub>3</sub>/P(VDF-TrFE) Composites. *Int. J. Appl. Ceram. Technol.* **2017**, *14*, 969–975. [[CrossRef](#)]
70. Bahrami, A.; Álvarez, J.P.; Depablos-Rivera, O.; Mirabal-Rojas, R.; Ruíz-Ramírez, A.; Muhl, S.; Rodil, S.E. Compositional and Tribo-Mechanical Characterization of Ti-Ta Coatings Prepared by Confocal Dual Magnetron Co-Sputtering. *Adv. Eng. Mater.* **2018**, *20*, 1700687. [[CrossRef](#)]
71. Konatu, R.T.; Silva, K.B.; da Silva Barros, F.; Claro, A.P.R.A. Análise Do Processamento Da Liga Ti<sub>30</sub>Ta Visando Aplicação Biomédica. *Arch. Health Investig.* **2014**, *5*, 235–240. [[CrossRef](#)]
72. Zhou, Y.L.; Niinomi, M.; Akahori, T. Decomposition of Martensite A'' during Aging Treatments and Resulting Mechanical Properties of Ti-Ta Alloys. *Mater. Sci. Eng. A* **2004**, *384*, 92–101. [[CrossRef](#)]
73. Rahmati, B.; Zalnezhad, E.; Sarhan, A.A.D.; Kamiab, Z.; Nasiri Tabrizi, B.; Abas, W.A.B.W. Enhancing the Adhesion Strength of Tantalum Oxide Ceramic Thin Film Coating on Biomedical Ti-6Al-4V Alloy by Thermal Surface Treatment. *Ceram. Int.* **2015**, *41*, 13055–13063. [[CrossRef](#)]
74. Matějček, J.; Vilémová, M.; Mušálek, R.; Sachr, P.; Horník, J. The Influence of Interface Characteristics on the Adhesion/Cohesion of Plasma Sprayed Tungsten Coatings. *Coatings* **2013**, *3*, 108–125. [[CrossRef](#)]
75. Quazi, M.M.; Ishak, M.; Arslan, A.; Nasir Bashir, M.; Ali, I. Scratch Adhesion and Wear Failure Characteristics of PVD Multilayer CrTi/CrTiN Thin Film Ceramic Coating Deposited on AA7075-T6 Aerospace Alloy. *J. Adhes. Sci. Technol.* **2018**, *32*, 625–641. [[CrossRef](#)]
76. Kusakabe, S.; Ralph Rawls, H.; Hotta, M. Relationship between Thin-Film Bond Strength as Measured by a Scratch Test, and Indentation Hardness for Bonding Agents. *Dent. Mater.* **2015**, *15*, 103–104. [[CrossRef](#)]
77. Harun, W.S.W.; Asri, R.I.M.; Alias, J.; Zulkifli, F.H.; Kadirgama, K.; Ghani, S.A.C.; Shariffuddin, J.H.M. A Comprehensive Review of Hydroxyapatite-Based Coatings Adhesion on Metallic Biomaterials. *Ceram. Int.* **2018**, *44*, 1250–1268. [[CrossRef](#)]
78. Rodrigues, L.F., Jr.; Tronco, M.C.; Escobar, C.F.; Rocha, A.S.; Santos, L.A.L. Painting Method for Hydroxyapatite Coating on Titanium Substrate. *Ceram. Int.* **2019**, *45*, 14806–14815. [[CrossRef](#)]
79. Hung, K.Y.; Lo, S.C.; Shih, C.S.; Yang, Y.C.; Feng, H.P.; Lin, Y.C. Titanium Surface Modified by Hydroxyapatite Coating for Dental Implants. *Surf. Coatings Technol.* **2013**, *231*, 337–345. [[CrossRef](#)]
80. Kikuchi, M.; Takada, Y.; Kiyosue, S.; Yoda, M.; Woldu, M.; Cai, Z.; Okuno, O.; Okabe, T. Mechanical Properties and Microstructures of Cast Ti-Cu Alloys. *Dent. Mater.* **2003**, *19*, 174–181. [[CrossRef](#)]
81. Nouri, A.; Wen, C. Introduction to Surface Coating and Modification for Metallic Biomaterials. In *Surface Coating and Modification of Metallic Biomaterials*; Elsevier Ltd.: Sawston, UK, 2015; pp. 3–60. ISBN 9781782423164.

82. Feng, B.; Weng, J.; Yang, B.C.; Qu, S.X.; Zhang, X.D. Characterization of Surface Oxide Films on Titanium and Adhesion of Osteoblast. *Biomaterials* **2003**, *24*, 4663–4670. [[CrossRef](#)]
83. Lai, H.C.; Zhuang, L.F.; Liu, X.; Wieland, M.; Zhang, Z.Y.; Zhang, Z.Y. The Influence of Surface Energy on Early Adherent Events of Osteoblast on Titanium Substrates. *J. Biomed. Mater. Res. Part A* **2010**, *93*, 289–296. [[CrossRef](#)]
84. Redey, S.A.; Razzouk, S.; Rey, C.; Bernache-Assollant, D.; Leroy, G.; Nardin, M.; Cournot, G. Osteoclast Adhesion and Activity on Synthetic Hydroxyapatite, Carbonated Hydroxyapatite, and Natural Calcium Carbonate: Relationship to Surface Energies. *J. Biomed. Mater. Res.* **1999**, *45*, 140–147. [[CrossRef](#)]
85. Paital, S.R.; Dahotre, N.B. Calcium Phosphate Coatings for Bio-Implant Applications: Materials, Performance Factors, and Methodologies. *Mater. Sci. Eng. R Rep.* **2009**, *66*, 1–70. [[CrossRef](#)]
86. Shen, L.; Gong, L.; Chen, S.; Zhan, S.; Zhang, C.; Shao, T. Improvement of  $\beta$ -Phase Crystal Formation in a BaTiO<sub>3</sub>-Modified PVDF Membrane. *Plasma Sci. Technol.* **2018**, *20*, 065510. [[CrossRef](#)]
87. Gittens, R.A.; Olivares-Navarrete, R.; Schwartz, Z.; Boyan, B.D. Implant Osseointegration and the Role of Microroughness and Nanostructures: Lessons for Spine Implants. *Acta Biomater.* **2014**, *10*, 3363–3371. [[CrossRef](#)]
88. Wilson, C.J.; Clegg, R.E.; Leavesley, D.I.; Pearcy, M.J. Mediation of Biomaterial–Cell Interactions by Adsorbed Proteins: A Review. *Tissue Eng.* **2005**, *11*, 1–18. [[CrossRef](#)]
89. Damiani, L.; Eales, M.G.; Nobbs, A.H.; Su, B.; Tsimbouri, P.M.; Salmeron-Sanchez, M.; Dalby, M.J. Impact of Surface Topography and Coating on Osteogenesis and Bacterial Attachment on Titanium Implants. *J. Tissue Eng.* **2018**, *9*, 204173141879069. [[CrossRef](#)] [[PubMed](#)]
90. Taherian, M.H.; Reza zadeh, M.; Taji, A. Optimum Surface Roughness for Titanium-Coated PEEK Produced by Electron Beam PVD for Orthopedic Applications. *Mater. Technol.* **2021**, *37*, 631–644. [[CrossRef](#)]
91. Besinis, A.; Hadi, S.D.; Le, H.R.; Tredwin, C.; Handy, R.D. Antibacterial Activity and Biofilm Inhibition by Surface Modified Titanium Alloy Medical Implants Following Application of Silver, Titanium Dioxide and Hydroxyapatite Nanocoatings. *Nanotoxicology* **2017**, *11*, 327–338. [[CrossRef](#)]
92. Wilson, W.W.; Wade, M.M.; Holman, S.C.; Champlin, F.R. Status of Methods for Assessing Bacterial Cell Surface Charge Properties Based on Zeta Potential Measurements. *J. Microbiol. Methods* **2001**, *43*, 153–164. [[CrossRef](#)]
93. Wu, X.; Ao, H.; He, Z.; Wang, Q.; Peng, Z. Surface Modification of Titanium by Femtosecond Laser in Reducing Bacterial Colonization. *Coatings* **2022**, *12*, 414. [[CrossRef](#)]
94. Pérez-Tanoira, R.; Han, X.; Soininen, A.; Aarnisalo, A.A.; Tiainen, V.M.; Eklund, K.K.; Esteban, J.; Kinnari, T.J. Competitive Colonization of Prosthetic Surfaces by Staphylococcus Aureus and Human Cells. *J. Biomed. Mater. Res. Part A* **2017**, *105*, 62–72. [[CrossRef](#)]
95. Nune, K.C.; Somani, M.C.; Spencer, C.T.; Misra, R.D.K. Cellular Response of Staphylococcus Aureus to Nanostructured Metallic Biomedical Devices: Surface Binding and Mechanism of Disruption of Colonization. *Mater. Technol.* **2017**, *32*, 22–31. [[CrossRef](#)]
96. Patel, S.S.; Aruni, W.; Inceoglu, S.; Akpolat, Y.T.; Botimer, G.D.; Cheng, W.K.; Danisa, O.A. A Comparison of Staphylococcus Aureus Biofilm Formation on Cobalt-Chrome and Titanium-Alloy Spinal Implants. *J. Clin. Neurosci.* **2016**, *31*, 219–223. [[CrossRef](#)]
97. Skovdal, S.M.; Jørgensen, N.P.; Petersen, E.; Jensen-Fangel, S.; Ogaki, R.; Zeng, G.; Johansen, M.I.; Wang, M.; Rohde, H.; Meyer, R.L. Ultra-Dense Polymer Brush Coating Reduces Staphylococcus Epidermidis Biofilms on Medical Implants and Improves Antibiotic Treatment Outcome. *Acta Biomater.* **2018**, *76*, 46–55. [[CrossRef](#)]
98. Zeng, G.; Ogaki, R.; Meyer, R.L. Non-Proteinaceous Bacterial Adhesins Challenge the Antifouling Properties of Polymer Brush Coatings. *Acta Biomater.* **2015**, *24*, 64–73. [[CrossRef](#)]
99. Wu, Y.; Zitelli, J.P.; TenHuisen, K.S.; Yu, X.; Libera, M.R. Differential Response of Staphylococci and Osteoblasts to Varying Titanium Surface Roughness. *Biomaterials* **2011**, *32*, 951–960. [[CrossRef](#)] [[PubMed](#)]
100. Lee, B.S.; Shih, K.S.; Lai, C.H.; Takeuchi, Y.; Chen, Y.W. Surface Property Alterations and Osteoblast Attachment to Contaminated Titanium Surfaces after Different Surface Treatments: An in Vitro Study. *Clin. Implant Dent. Relat. Res.* **2018**, *20*, 583–591. [[CrossRef](#)] [[PubMed](#)]
101. Cerca, N.; Pier, G.B.; Vilanova, M.; Oliveira, R.; Azeredo, J. Quantitative Analysis of Adhesion and Biofilm Formation on Hydrophilic and Hydrophobic Surfaces of Clinical Isolates of Staphylococcus Epidermidis. *Res. Microbiol.* **2005**, *156*, 506–514. [[CrossRef](#)]
102. Lerebour, G.; Cupferman, S.; Bellon-Fontaine, M.N. Adhesion of Staphylococcus Aureus and Staphylococcus Epidermidis to the Episkin®Reconstructed Epidermis Model and to an Inert 304 Stainless Steel Substrate. *J. Appl. Microbiol.* **2004**, *97*, 7–16. [[CrossRef](#)]
103. Sousa, C.; Teixeira, P.; Oliveira, R. Influence of Surface Properties on the Adhesion of Staphylococcus Epidermidis to Acrylic and Silicone. *Int. J. Biomater.* **2009**, *2009*, 718017. [[CrossRef](#)]
104. Cuello, E.A.; Mulko, L.E.; Barbero, C.A.; Acevedo, D.F.; Yslas, E.I. Development of Micropatterning Polyimide Films for Enhanced Antifouling and Antibacterial Properties. *Colloids Surfaces B Biointerfaces* **2020**, *188*, 110801. [[CrossRef](#)] [[PubMed](#)]
105. Yang, K.; Shi, J.; Wang, L.; Chen, Y.; Liang, C.; Yang, L.; Wang, L.N. Bacterial Anti-Adhesion Surface Design: Surface Patterning, Roughness and Wettability: A Review. *J. Mater. Sci. Technol.* **2022**, *99*, 82–100. [[CrossRef](#)]